Article

Not peer-reviewed version

Formation Conditions of Extremely Reduced High-Temperature Mineral Assemblages in Rocks of Combustion Metamorphic Complexes (Mongolia)

Igor S. Peretyazhko * and Elena A. Savina

Posted Date: 18 October 2024

doi: 10.20944/preprints202410.1443.v1

Keywords: reduced mineral assemblages; troilite; iron phosphide; metallic iron; wüstite; magnesiowüstite–ferropericlase; Raman spectroscopy; combustion metamorphic complex; Mongolia

Article

Formation Conditions of Extremely Reduced High-Temperature Mineral Assemblages in Rocks of Combustion Metamorphic Complexes (Mongolia)

Igor S. Peretyazhko * and Elena A. Savina

Vinogradov Institute of Geochemistry, Russian Academy of Sciences, Siberian Branch, 664033 Irkutsk, Russia
* Correspondence: pgmigor@igc.irk.ru

Abstract: New data, including Raman spectroscopy, characterize unusual mineral assemblages from rocks of the Naylga and Khamaryn–Khyral–Khiid combustion metamorphic complexes in Mongolia. Several samples of melilite–nepheline paralava and other thermally altered (metamorphosed) sedimentary rocks contain troilite (FeS), metallic iron (Fe^0), kamacite (Ni-bearing Fe^0), taenite (Ni-rich Fe^0), barringerite or allobogdanite (Fe_2P), schreibersite (Fe_3P), steadite (Fe_4P = eutectic α-Fe+Fe_3P), wüstite (FeO), and cohenite (Fe_3C). The paralava matrix includes a fragment composed of magnesiowüstite–ferropericlase (FeO–MgO solid solution), as well as of spinel $(Mg,Fe)Al_2O_4$ and forsterite. The highest-temperature mineral assemblage belongs to a xenolithic remnant, possibly Fe-rich sinter: molten ash left after underground combustion of coal seams. The crystallization temperatures of the observed iron phases were estimated using phase diagrams for the respective systems: Fe–S for iron sulfides and Fe–P for iron phosphides. Iron monosulfide (high-temperature pyrrhotite) with inclusions of Fe^0 underwent solid-state conversion into troilite at 140 °C. Iron phosphides in inclusions from the early growth zone of anorthite–bytownite in melilite–nepheline paralava crystallized from < 1370 to 1165 °C (Fe_2P), 1165–1048 °C (Fe_3P), and <1048 °C (Fe_4P). Phase relations in zoned spherules consisting of troilite + Fe^0 (or kamacite, taenite) + Fe_3P ± (Fe_3C, Fe_4P) reveal potential presence of a homogeneous Fe–S–P–C melt at T ~1350 °C, which separated into two immiscible melts in the 1350–1250 °C range, namely, a dense Fe–P–C melt in the core and a less dense Fe–S melt in the rim. The melts evolved in accordance with cooling paths in the Fe–S and Fe–P–C phase diagrams. Cohenite and schreibersite in the spherules crystallized between 988 °C and 952 °C. The crystallization temperatures of minerals were used to reconstruct redox patterns with respect to the CCO, IW, IM, and MW buffer equilibria during melting of marly limestone and subsequent crystallization and cooling of melilite–nepheline paralava melts. The origin of the analyzed CM rocks was explained in a model implying thermal alteration of low-permeable overburden domains in reducing conditions during wild subsurface coal fires, while heating was transferred conductively from adjacent parts of ignited coal seams. The gas regime in the zones of combustion was controlled by the CCO buffer at excess atomic carbon. Paralava melts exposed to high-temperature extremely reducing conditions contained droplets of immiscible Fe–P–S–C, Fe–S, Fe–P, and Fe–P–C liquids which then crystallized to reduced mineral assemblages.

Keywords: reduced mineral assemblages; troilite; iron phosphide; metallic iron; wüstite; magnesiowüstite–ferropericlase; Raman spectroscopy; combustion metamorphic complex; Mongolia

1. Introduction

The East Mongolian coal province in central and eastern Mongolia accommodates the Nyalga and Khamaryn–Khyral–Khiid combustion metamorphic (CM) complexes consisting of thermally metamorphosed and partly melted rocks produced by multi-stage Quaternary and modern wild fires of coal stored in Early Cretaceous sediments. We discovered the two complexes in 2016–2018 and have been studying them since then. The history of discoveries and an inventory of the available data on local geology, lithology, and mineralogy of main rock types were reported in our previous publications [1–8].

 doi:10.20944/preprints202410.1443.v1

The Nyalga complex consists of more or less strongly thermally altered pelitic sediments and products of their partial melting (paralavas and vitreous clinker) exposed in three ≤ 40 m high erosion outliers [1,2]. Melilite–nepheline paralava containing minerals of the rhönite–kuratite series occurs as scattered rock fragments or single blocks on the outliers or on eroded surfaces nearby [1]. Clinker and paralavas in the area often enclose xenoliths of burnt sedimentary rocks. Signatures of CM alteration in sediments were also found in the Tugrug coal quarry located 4–5 km southeast of the outliers [2].

The territory of the Khamaryn–Khyral–Khiid complex has a rugged topography typical of coal fire areas, with long ridges, numerous gullies, fissures, and caves produced by weathering and collapse of overburden above combusted coal seams [3]. No active coal combustion has been observed lately though a focus of underground smoldering remains in the zone of the last coal fire of 1932–1947, where erosion stripped warm CM rocks.

The CM rocks are remarkable by high diversity of mineral assemblages due to the lithology of the sedimentary protoliths and local conditions of multi-stage thermal alteration and partly melting. The two complexes consist of predominant CM pelitic sediments and vitreous clinker of various compositions, as well as mineralogically exceptional melilite–nepheline paralava. The paralava mineralogy includes basic plagioclase, clinopyroxene, and melilite in phenocrysts, with interstitial nepheline and high-silica potassic glass that encloses olivine group minerals (Ca-bearing fayalite, kirschsteinite), spinel, K-Ba feldspars (celsian, hyalophane), and other phases, including very rare ones [1–5]. The CM complexes also contain much less abundant paralavas of plagioclase–pyroxene ± indialite (Naylga complex), sekaninaite–tridymite, and cristobalite–fayalite (Khamaryn–Khyral–Khiid complex) main mineral compositions.

The Khamaryn–Khyral–Khiid CM rocks host remnant marly limestone in which calcite and silicate minerals melted successively at elevated CO_2 partial pressure and $T > 1250$ °C, with formation of carbonate and Ca-rich silicate mafic melts crystallized then into melilite–nepheline paralava [6]. The Khamaryn–Khyral–Khiid cristobalite clinker and tridymite–sekaninaite and cristobalite–fayalite paralava compositions were formed by partial melting of pelites in a large temperature interval [4]. Mullite crystallized in abundance at $T > 850$°C after dehydration-dehydroxylation and incongruent melting of amorphous pelitic material. The sedimentary overburden above coal fire foci heated up to $T > 1050$°C (as inferred from crystallization temperatures of cordierite-group minerals), or locally even to $T > 1470$°C required for melting of detrital quartz and possibly corresponding to the stability field of β-cristobalite [5].

The studies of CM rocks in the area continue. We report new data concerning unusual high-temperature reduced mineral assemblages found sporadically in the Naylga and Khamaryn–Khyral–Khiid complexes. Some melilite–nepheline paralava and clinker samples bear troilite (FeS), metallic iron (Fe^0), kamacite (Ni-bearing Fe^0), taenite (Ni-rich Fe^0), iron phosphides (barringerite or allobogdanite Fe_2P, schreibersite Fe_3P, and steadite Fe_4P = eutectic α-Fe + Fe_3P), as well as wüstite (FeO), and cohenite (Fe_3C). Raman spectroscopy of the constituent minerals revealed schreibersite, cohenite, wüstite, magnesiowüstite–ferropericlase, magnetite, minerals of pyroxene, olivine, cordierite, and spinel groups, rhönite–kuratite series, melilite, nepheline, cristobalite, troilite, pyrrhotite, marcasite, goethite, ferropseudobrookite-pseudobrookite, and rutile.

The crystallization conditions of magnesiowüstite–ferropericlase, Fe^0, iron monosulfide with Fe^0 inclusions, wüstite + magnetite, iron phosphides (Fe_2P, Fe_3P, and Fe_4P) + Fe_3C were reconstructed using the Fe–S, MgO–FeO, MgO–FeO–Al_2O_3, Fe–P, Fe–P–C, and Fe–S–P phase diagrams. The obtained temperature estimates were used to infer the redox conditions with respect to the CCO, IW (Iron–Wüstite), IM (Iron–Magnetite), and MW (Magnetite–Wüstite) buffer equilibria during melting of marly limestone and crystallization of melilite–nepheline paralava melts. The origin of the analyzed CM rocks was explained in a model implying thermal alteration in locally reducing conditions of low-permeable sedimentary overburden above foci of wild subsurface coal fires.

2. Materials and Methods

 doi:10.20944/preprints202410.1443.v1

The collected samples were analyzed at the Center for Isotope-Geochemical Studies of the Vinogradov Institute of Geochemistry, Siberian Branch of the Russian Academy of Sciences (IGC, Irkutsk). Mineralogy and phase compositions were investigated by scanning electron microscopy coupled with energy-dispersive spectrometry (SEM EDS) on a *Tescan Mira* 3 LMU microscope with an *ULTIM MAX 40* microanalysis system (Oxford Instruments). The analyses were performed in a scanning mode on carbon-coated polished cut surfaces of samples, at 1 to and over > 10 μm² spots, 20 kV accelerating voltage, 1 nA beam current, and 30 s acquisition time (excluding dead time). Carbon in cohenite was identified in some gold-sputtered samples. The data quality was checked against analyses of reference samples, including quartz, albite, orthoclase, wollastonite, MgO, Al_2O_3, CaF_2, metals, and synthetic compounds from sets 6316 and 7682 of the reference standards by Microanalysis Consultants Limited (Oxford Instruments Ltd., UK). All the calculations and matrix corrections were conducted automatically in *AZtec* (software of Oxford Instruments Nanoanalysis, UK). The detection limits of major elements were 0.2–0.3 wt%. Average random errors varied from 0.9 tp 13 rel% depending on major-element contents: ± 0.9 rel% at > 10 wt%, ± 3.0 rel% at 1–10 wt%, and ± 13 rel% at 0.3–1 wt% [9]. The crystal chemical formulas were calculated using the *Crystal* software, ver. 3.0 [10].

The Raman spectra were collected on a *WITec* confocal *Alpha 300R* (WITec GmbH) spectrometer with 532 nm Nd:YAG laser (power 0.5–17 mW), at the Analytical Center for Geodynamics and Geochronology in the Institute of the Earth's Crust (Irkutsk). The 1–2 μm laser beam was focused using a 100x Carl Zeiss lens. The range of the used Raman shift regions was from 100–3600 cm^{-1}. The data was calibrated against a silicon peak of 520.7 cm^{-1} at an optical resolution of 1800 grooves/mm and 600 grooves/mm groove densities. Spectral acquisition time was from 1 to 10 s. Total spectra with 20–100 (up to 5400) accumulations were collected for each measurement. The spectra were processed without baseline correction in the ArDI system of mineral vibrational spectroscopy data processing and analysis [11]. Mineral phases were identified with reference to the RRUFF database (http://rruff.info/) [12] (last accessed on 15 October 2024) and to published data.

3. Results

3.1. Identification of Minerals

Minerals in > 2 μm inclusions were identified from Raman spectra and SEM-EDS data. The previously obtained Raman spectra for a number of rare phases from CM rocks in Mongolia revealed minerals of several groups, including rhönite–kuratite [1], cordierite (orthorhombic cordierite and sekaninaite, hexagonal indialite and ferroindialite), silica polymorphs (cristobalite and tridymite), and spinel-group minerals (including silicate spinel), as well as mullite and Fe-rich mullite [3–5]. Raman spectra were also used to identify iron sulfides, iron oxides, and several silicate minerals (see some examples in Figure 1).

It was problematic to discriminate between pyrrhotite $Fe_{1-x}S$ $(x= 0\text{-}0.17)$ and troilite FeS iron monosulfides which have minor difference in iron and sulfur contents (62.33 against 63.53 wt% Fe and 37.67 against 36.47 wt% S, respectively). The Raman spectra of iron monosulfides were acquired at different laser power values. The monosulfide surface was heated at laser power increasing from 1 to 17 mW, with successive oxidation $FeS + O_2 \rightarrow Fe_3O_4 + SO_2$; $FeO + O_2 \rightarrow Fe_2O_3 + SO_2$ in the laser-exposed zone [13]. As a result, the spectra showed peaks of magnetite and hematite from an oxide film formed on the monosulfide surface (Figure 2).

 doi:10.20944/preprints202410.1443.v1

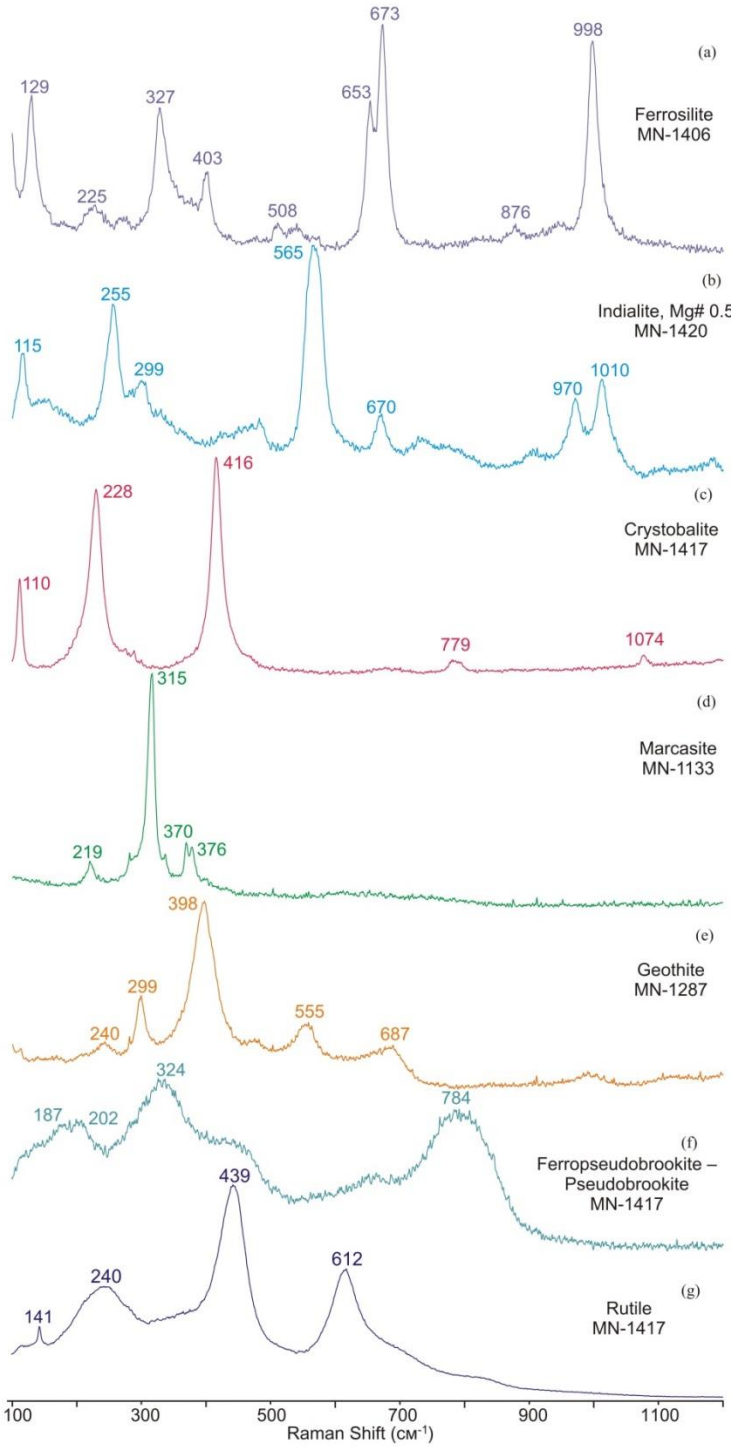

Figure 1. Raman spectra of several minerals from CM rocks.

Similar shapes and trends in the Raman spectra changing as a function of laser power and temperature are typical of many iron-rich sulfide and oxide phases, such as pyrite, magnetite, goethite, etc. [13], as well as schreibersite (our data). Therefore, the Raman spectroscopy was performed at the lowest laser power and prolonged acquisition time from 10 minutes to 3 hours. However, the Raman spectra of troilite and pyrrhotite were poorly discriminable even at those operation conditions because of weak peaks in the characteristic region of 100 to 400 cm^{-1}. The peaks of troilite are known to be small in the 148–331 cm^{-1} interval [13] while those of pyrrhotite are

 doi:10.20944/preprints202410.1443.v1

relatively high at 314 and 372 cm^{-1} (RRUFF, [12]), but the spectra we collected lack these bands (Figure 2b). Thus, the iron monosulfide grains in the samples studied by Raman spectroscopy must be troilite.

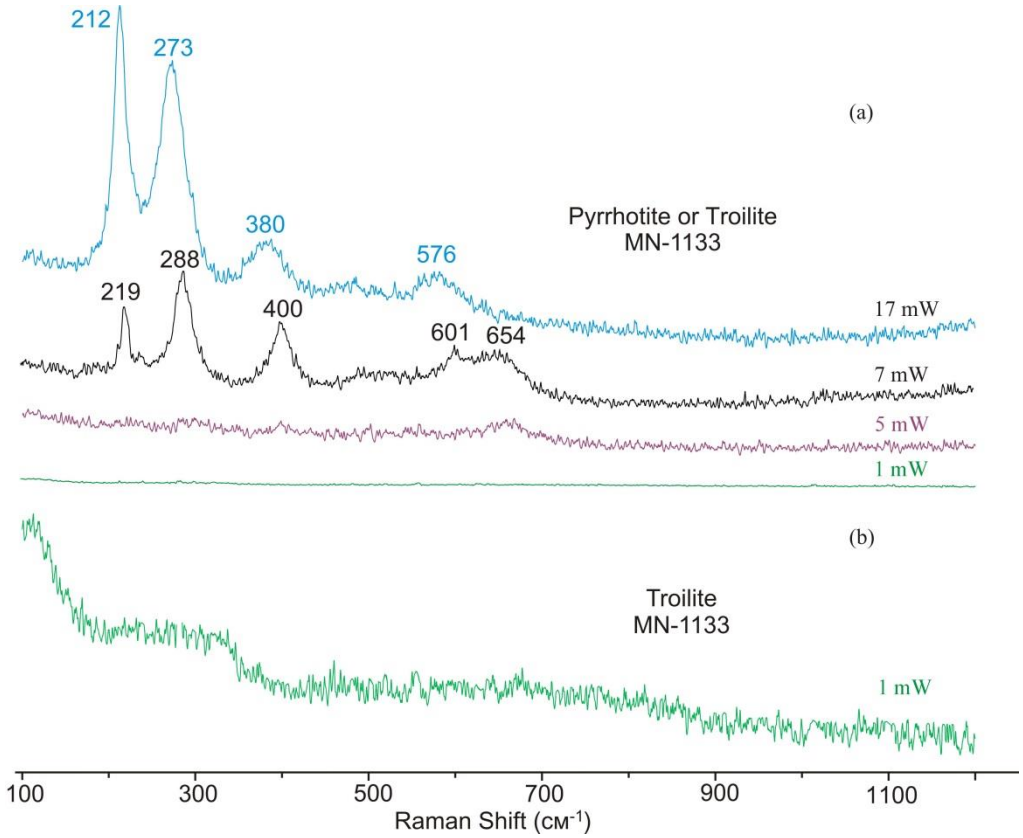

Figure 2. (a): Raman spectra of iron monosulfide (pyrrhotite or troilite) and its oxidation products collected at a laser power of 5, 7, and 17 mW; (b): spectrum of troilite acquired at 1 mW laser power, 5400 accumulations to 2 s (3 hrs).

Iron sulfides can be successfully identified using the Fe–S phase diagram. The Fe–S system at ambient pressure has been largely studied, but the available phase diagrams differ significantly, especially in the T < 400 °C region [14,15] and references therein]. Best consistency was achieved in the diagram based on thermodynamic modeling and experimental evidence (Figure 3). In addition to the FeS and FeS_2 phases, the Fe–S system produce several non-stoichiometric phases with the common formula $Fe_{1-x}S$. At P = 1 bar and T > 1000 °C, the phase diagram displays fields of an Fe–S melt, face-centered cubic (fcc) iron (γ-Fe), body-centered-cubic (bcc) iron (α-Fe), and hexagonal pyrrhotite. The latter is a hexagonal monosulfide having an NiAs structure and non-stoichiometric excess of S ($Fe_{1-x}S$), which melts congruently at ~1190 °C. Pyrite (FeS_2), with its highest S enrichment in the Fe–S system, undergoes incongruent melting at 743 °C to produce pyrrhotite $Fe_{1-x}S$ and an almost pure S melt. The compositions between stoichiometric troilite (FeS) and monoclinic pyrrhotite (Fe_7S_8) were constrained only qualitatively in terms of phase relations at T < 320 °C. Troilite is a FeS polymorph stable at T < 140 °C and rarely found in terrestrial rocks. The iron monosulfide known from mineral assemblages with Fe^0 in stony-iron and iron meteorites is also commonly referred as troilite. The troilite converts into hexagonal pyrrhotite at temperatures above 140 °C.

The mineral assemblages of melilite–nepheline paralava in the sampled CM complexes of Mongolia typically include a phase with its composition close or corresponding to FeS [2,3]. Proceeding from the Fe–S phase diagram (Figure 3) and the Raman spectra (Figure 2b), troilite in this study refers to iron monosulfide grains, globules, and spherules associated with Fe^0, while other monosulfide phase are identified as pyrrhotite.

 doi:10.20944/preprints202410.1443.v1

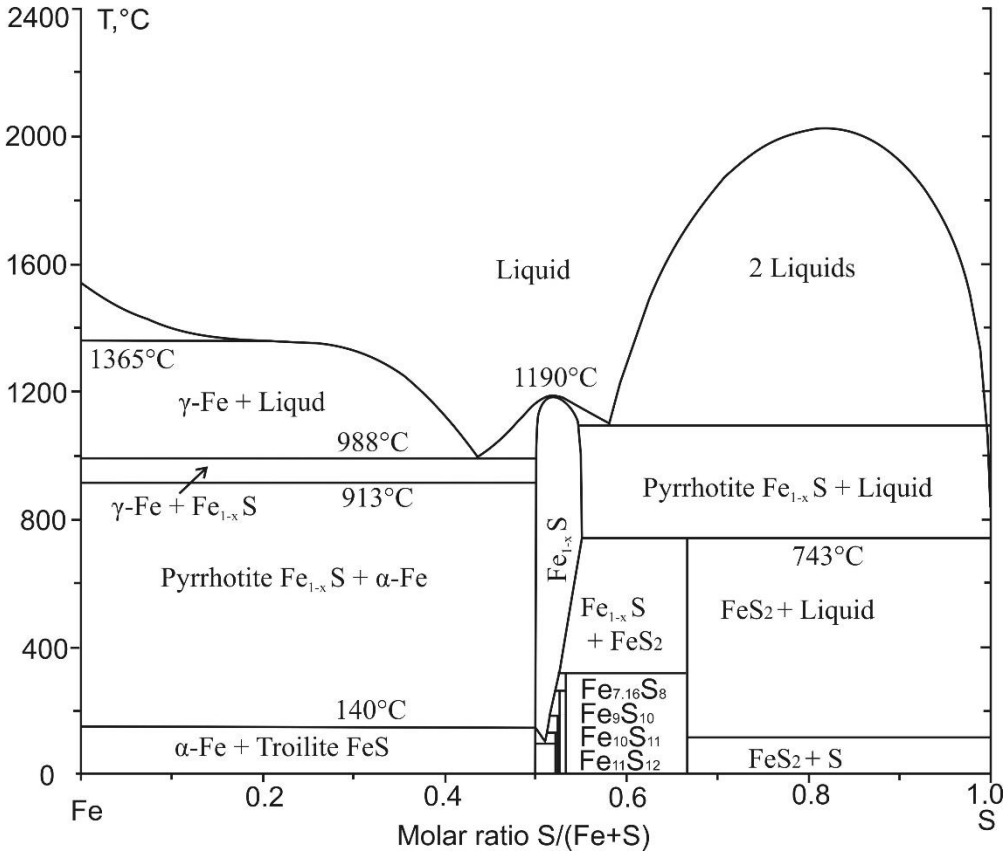

Figure 3. Phase diagram of the Fe–S system, after Waldner and Pelton [14] and Shishin et al. [15].

Raman spectroscopy data on iron phosphides, including schreibersite (Fe_3P), barringerite or allobogdanite (Fe_2P), and steadite (Fe_4P = eutectic α-Fe + Fe_3P), are absent or poorly consistent [16]. Only schreibersite can be identified from its Raman spectrum similar to that in the RRUFF database. At a small laser power, the spectra of Fe_3P contain several peaks in the 100–200 cm^{-1} region and a typical trough between 400 and 700 cm^{-1} (Figure 4a). The phase identification of other phosphides (Fe_2P and Fe_4P) was based on the Fe/P ratio from SEM-EDS data.

Cohenite Fe_3C was identified in several 2–4 μm inclusions by Raman spectroscopy (Figure 4b) and SEM-EDS analysis of gold-sputtered samples (see below). The Raman spectrum of Fe/Fe_3C shows D and G bands at 1330–1560 cm^{-1} which correspond to structural defects/disorder and are associated with first-order scattering of carbon domains characteristic of graphite-like materials. The presence of Fe_3C is also detectable from several peaks between 100 and 300 cm^{-1} usually attributed to stretching vibration modes between metal and carbon atoms [17].

Kamacite (Ni-bearing α-Fe), taenite (Ni-rich α-Fe), wüstite, and rare sulfides, such as ninengerite (Mn,Fe)S, cubanite $CuFe_2S_3$, nukundamite $Cu_2Fe_2S_4$, and bornite Cu_5FeS_4, were provisionally identified according to their compositions and related stoichiometric formulas.

 doi:10.20944/preprints202410.1443.v1

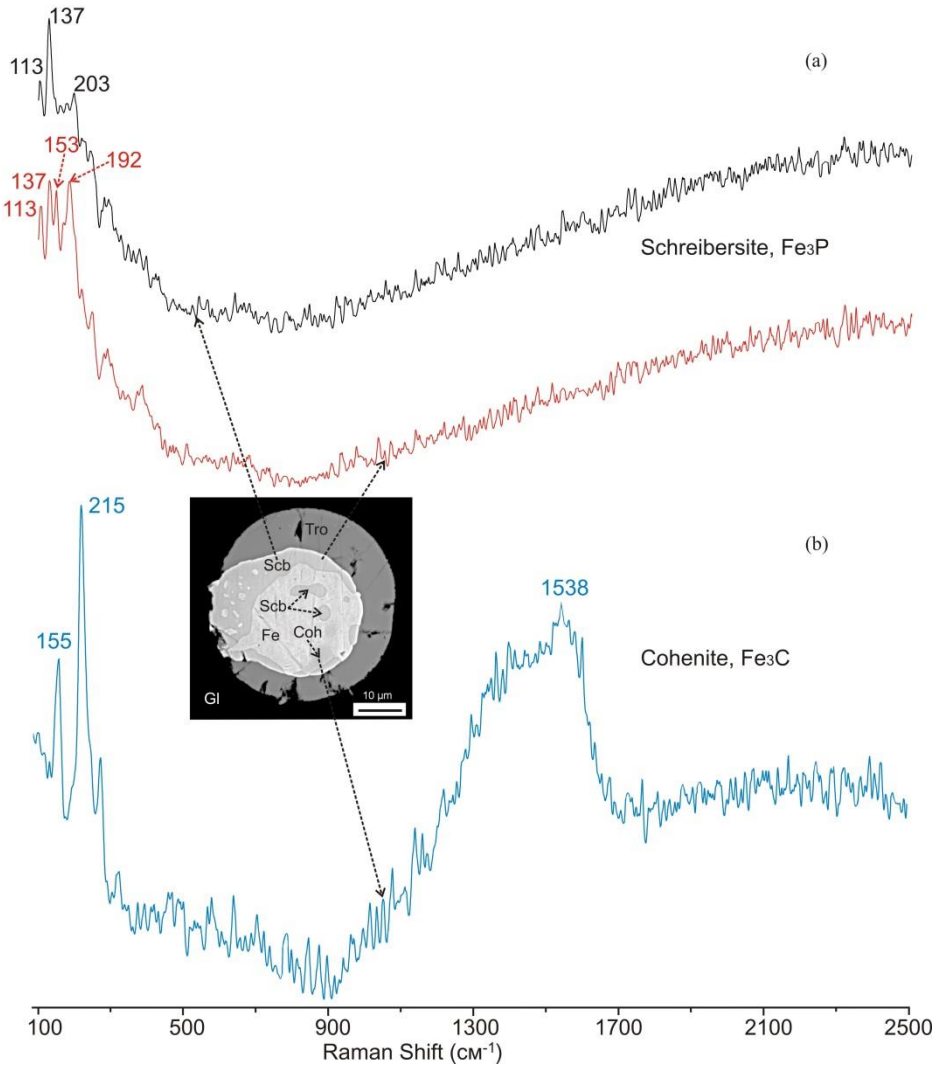

Figure 4. Raman spectra of schreibersite Fe_3P (a) and cohenite Fe_3C (b). Operation conditions: laser power 5 mW, 600 accumulations to 1 s, groove density 600 gr/mm (a) and laser power 5 mW, 1000 accumulations to 1 s, groove density 600 gr/mm (b).

3.2. Reduced Mineral Assemblages in Rocks of the Nyalga CM Complex

The mineralogy of melilite–nepheline and plagioclase–pyroxene ± indialite paralavas in the Nyalga complex was described in our previous publications [1,2]. The matrix of the Nyalga paralavas often encloses iron monosulfide, but small spherules and round grains of troilite with Fe^0 inclusions were found only in three out of twenty five samples. Some samples of melilite–nepheline paralava also host coarse (up to 3×5 mm) grains of troilite with Fe^0 inclusions and veinlets filled with wüstite, magnetite, and goethite. Troilite in those samples was identified according to Raman spectra, as well as proceeding from the association with Fe^0 and with replacing wüstite and magnetite.

Melilite–nepheline paralava in sample MN-1287 bears a coarse troilite grain cut by numerous symplectitic zones with inclusions of wüstite replaced by pure stoichiometric magnetite (Figure 5). The Raman spectra of wüstite differ from those of magnetite in smaller peaks at ~550 and ~670 cm^{-1} in the 500–700 cm^{-1} range (Figure 6a). In zones near cracks, wüstite is almost fully replaced by magnetite while the latter, in turn, becomes replaced by goethite (see its Raman spectrum in Figure 1e). Troilite near cracks in rims is often replaced by FeS_2 sulfide which has its Raman spectrum similar to marcasite (Figures 1d, 5b,c,e). Symplectitic zones sometimes enclose goethite and (Mg,Mn)-bearing siderite (Figure 5f).

 doi:10.20944/preprints202410.1443.v1

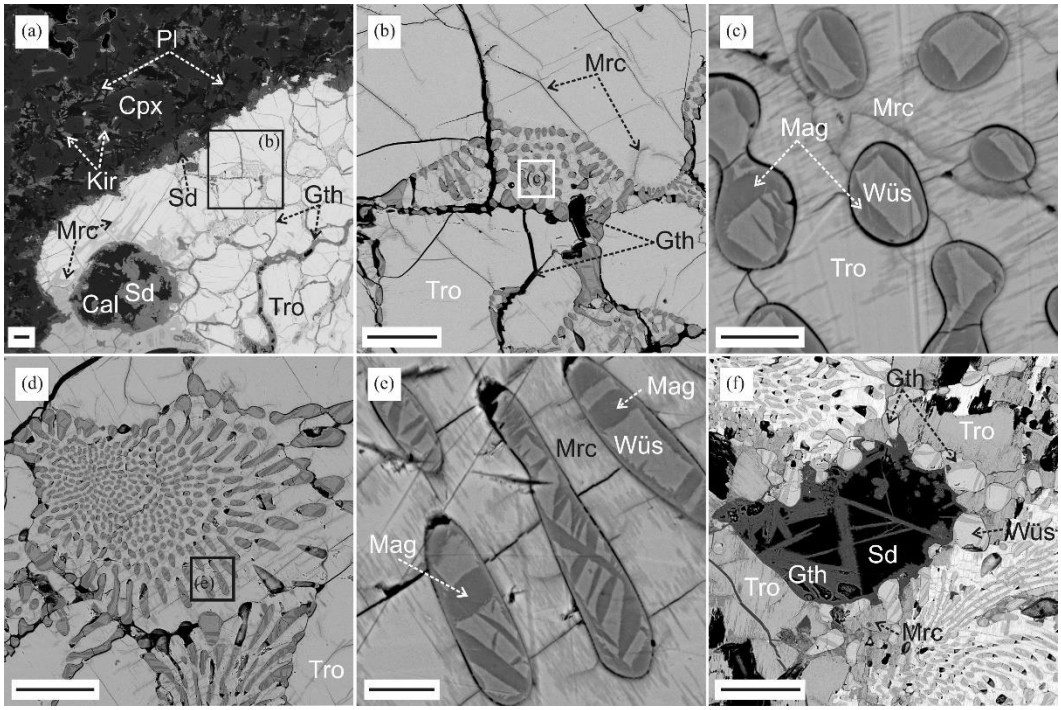

Figure 5. Fragments of a coarse troilite grain in sample MN-1287, with enlarged symplectitic zones. Scale bars: 10 μm in panels (c,e) and 100 μm in panels (a,b,d,f) Fragments of a coarse troilite grain in sample MN-1287, with enlarged symplectitic zones. Scale bars: 10 μm in panels (c,e) and 100 μm in panels (a,b,d,f). Abbreviations stand for Tro = troilite, Mag = magnetite Wüs = wüstite, Mrc = marcasite, Gth = goethite, Sd = siderite, Cal = calcite, Cpx = clinopyroxene, Pl = plagioclase, Kir = kirschsteinite.

The exposed surface of a large troilite grain in melilite–nepheline paralava sample MN-1133 displays sporadic inclusions of Fe^0 rimmed with stoichiometric magnetite. Numerous cracks in the grain are filled with wüstite which is replaced by magnetite along undeformed zones (Figure 7a-d). In cracks, magnetite is partly or fully replaced by goethite, while troilite is partly replaced by marcasite (Figure 7a); iron sulfate (calculated per formula Fe_2SO_4) occurs near some cracks.

The matrix of sample MN-1133 is locally composed of a mineral assemblage unusual for melilite–nepheline paralava, with grains of spinel $(Mg,Fe)Al_2O_4$ and forsterite, as well as Fe-Mg oxide, up to 15–20 μm in the large dimension, and with disseminated magnesioferrite $(Mg,Fe^{2+})(Fe^{3+})_2O_4$ at grain boundaries or in the grain interior (Figure 7e-g). The Fe-Mg oxide grains contain 42–74 wt% FeO and 59–25% MgO; the total reaches 100 wt%, and the FeO/(FeO + MgO) ratio is 0.42–0.74, or 0.3–0.6 apfu Fe^{2+} as calculated per solid solution $(Fe^{2+},Mg)O$ of wüstite–periclase or magnesiowüstite–ferropericlase (Figure 7e-g, Table 1, an. 1, 2). Fe-Mg oxide of this composition does not fit the formula of magnesioferrite; it appears as a crystalline phase in its Raman spectrum (Figure 6b). The spectra show strong peaks in the 100–200 cm^{-1} range and two gentle peaks at ~600 and ~1200 cm^{-1}. Note that the characteristic peaks in the spectra of wüstite and magnetite from inclusions in symplectitic zones hosted by troilite in sample MN-1287 likewise fall within the 500–700 cm^{-1} range (Figure 6).

 doi:10.20944/preprints202410.1443.v1

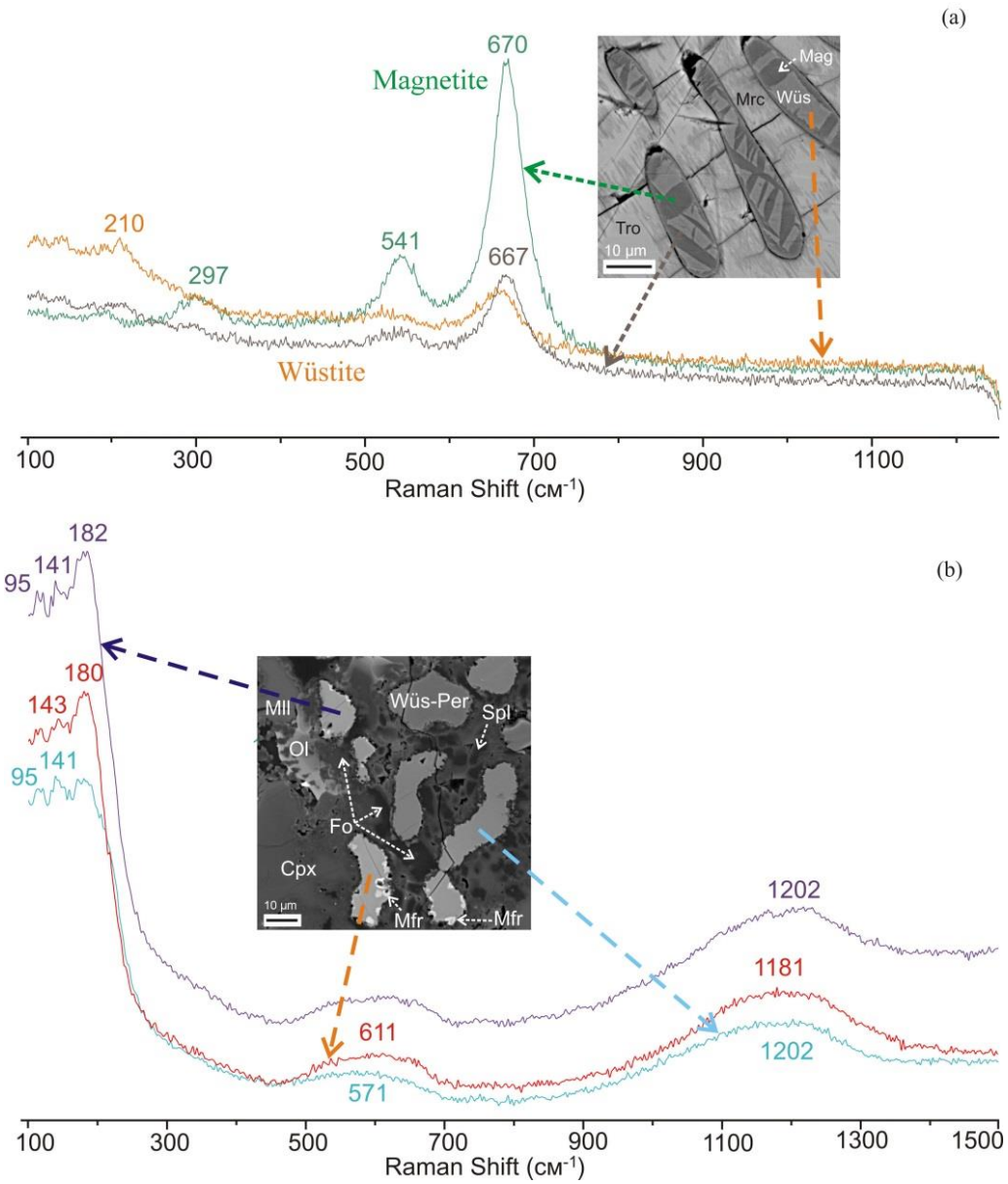

Figure 6. Raman spectra of magnetite and wüstite from sample MN-1287 (a) and ferropericlase–magnesiowüstite from sample MN-1133. Operation conditions: laser power 1–5 mW, 600 accumulations to 1 s, groove density 1800 gr/mm (a) and laser power 5 mW, 1000 accumulations to 1 s, groove density 600 gr/mm (b).

 doi:10.20944/preprints202410.1443.v1

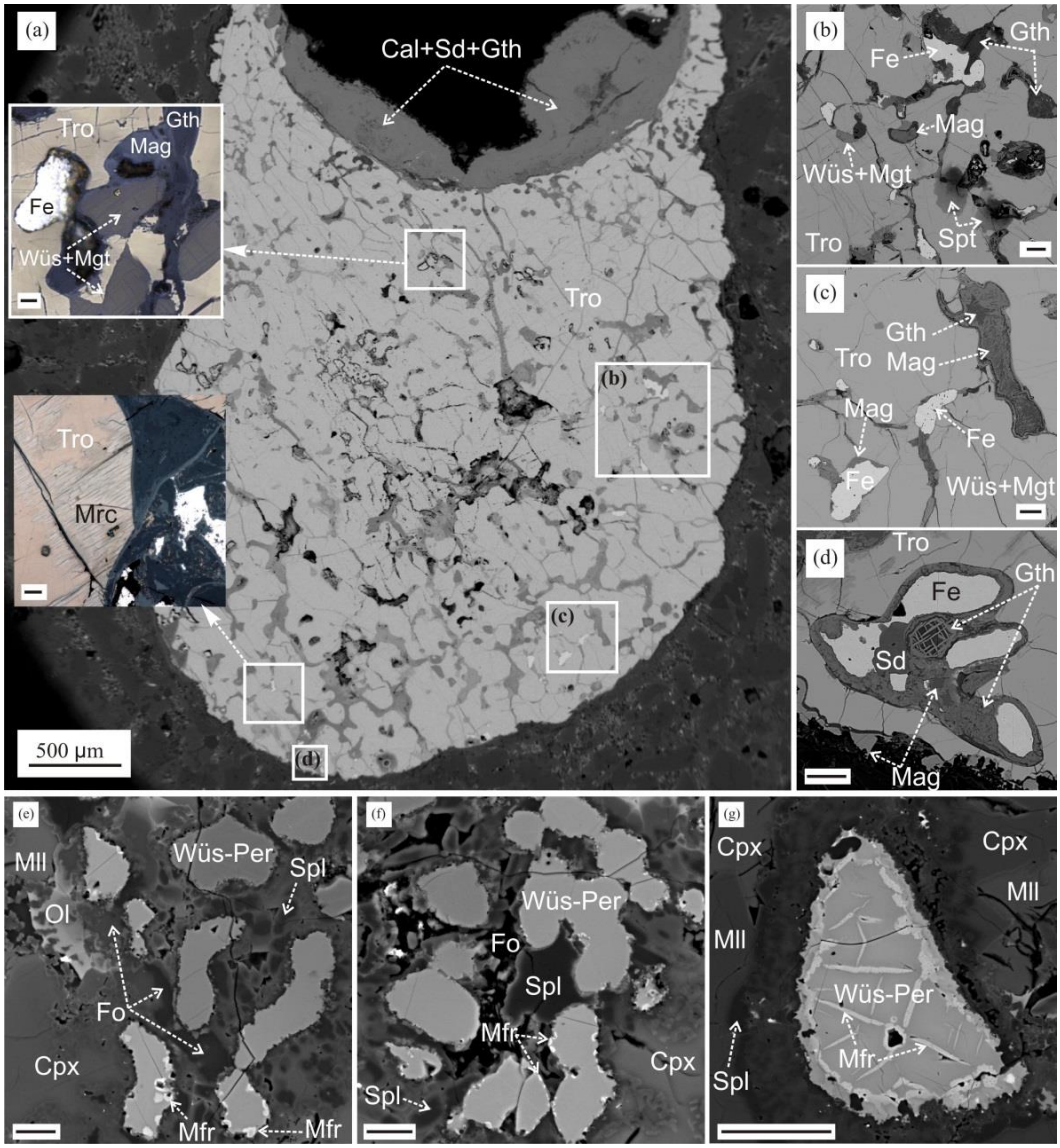

Figure 7. Fragments of a coarse troilite grain in sample MN-1133, with some enlarged zones (a-d) and mineral assemblages with magnesiowüstite–ferropericlase (e-g). Scale bars: 10 µm in panels (e,f) and 40 µm in panels (a-d,g) for BSE images. Abbreviations stand for Tro = troilite, Fe = metallic iron, Wüs-Per = magnesiowüstite–ferropericlase, Mfr = magnesioferrite, Mag = magnetite, Mrc = marcasite, Gth = goethite, Fo = forsterite, Ol = Mg-Fe olivine, Pl = plagioclase, Cpx = clinopyroxene, Mll = melilite, Spl = spinel, Sd = siderite, Cal = calcite.

 doi:10.20944/preprints202410.1443.v1

Table 1. Selected chemical compositions and calculated formulae of magnesiowüstite–ferropericlase (1,2), sulfides (3–5), metallic iron (6), kamacite (7), taenite (8), cohenite (9), and iron phosphides (10–15).

Major components, wt%														
	W-P		Tro	Cub	Nng	Fe^0	Kam	Tae	Coh	Fe_2P	Fe_3P			Fe_4P
	1	**2**	**3**	**4**	**5**	**6**	**7**	**8**	**9**	**10**	**11**	**12**	**13**	**14**	**15**
Mg	57.82*	28.21*													
Mn	0.41*	0.56*		0.35	29.11										
Fe	42.21*	71.90*	62.63	39.59	35.14	95.05	88.32	73.25	92.99	74.90	84.64	81.03	71.29	60.91	86.00
Ni				0.98				21.08				1.48	11.74	20.39	0.76
Co							2.50	2.62		0.67	0.72	0.77	1.83	2.63	
Cu				25.38			0.79	0.40							
As							0.44	1.27							
P						0.70	0.66			23.66	15.10	15.20	14.29	14.93	10.65
S			36.98	33.78	37.06		0.79						0.30	0.30	
C									6.67**						
Total	100.45	100.67	99.61	100.08	101.31	96.75	100.02	98.62	99.66	99.23	100.27	98.50	99.45	99.15	97.41
Chemical formula (apfu) **															
Mg	0.707	0.410													
Mn	0.003	0.005		0.017	0.458										
Fe	0.290	0.585	0.986	1.947	0.544	0.987	0.879	0.755	3	1.901	3.006	2.931	2.593	2.221	4.059
Ni				0.046			0.062	0.207				0.051	0.406	0.707	0.034
Co							0.024	0.026		0.016	0.024	0.026	0.063	0.091	
Cu				1.097			0.007	0.004							
As							0.003	0.010							
P						0.013	0.012			1.083	0.969	0.991	0.937	0.981	0.906
S			1.014	2.893	0.999		0.014								
C									1						
Sum	1	1	2	6	2	1	1	1	4	3	4	4	4	4	5

Note. *values for oxides; **values calculated based on assumed total number of atoms per formula unit quoted in the bottom row. Dash stands for concentrations below detection limit. W-P = magnesiowüstite–ferropericlase, Tro = troilite, Cub = cubanite, Nng = Fe-dominant analogue of ninengerite, Fe^0 = metallic iron, Kam = kamacite, Tae = taenite, Coh = cohenite, Fe_2P = barringerite or allabogdanite, Fe_3P = schreibersite, Fe_4P = steadite.

 doi:10.20944/preprints202410.1443.v1

3.3. Reduced Mineral Assemblages in Rocks of the Khamaryn–Khural–Khiid Complex

The analyzed samples from the Khamaryn–Khural–Khiid complex were melilite–nepheline and ferroan (tridymite–sekaninaite and cristobalite–fayalite) paralavas, as well as crystobalite clinker and vitreous rocks produced by partial melting of pelitic rocks [3–5].

Sample MN-1417 is mostly glass that hosts numerous xenoliths of vitreous clinker and molten pelite (possibly, mudstone), abundant partially dissolved or fused grains of detrital quartz, and rare grains of zircon and ferropseudobrookite–pseudobrookite with rutile inclusions (Figure 8). Quartz grains are densely cut by veinlets filled with cristobalite. Other inclusions in glass are numerous clusters of submicrometer magnetite, small acicular mullite and Fe-rich mullite (< 2–3 μm in the long dimension), and round globules of metallic iron or troilite with Fe^0 inclusions, as well as zoned spherules, up to 100–150 μm in diameter (Figures 8 and 9).

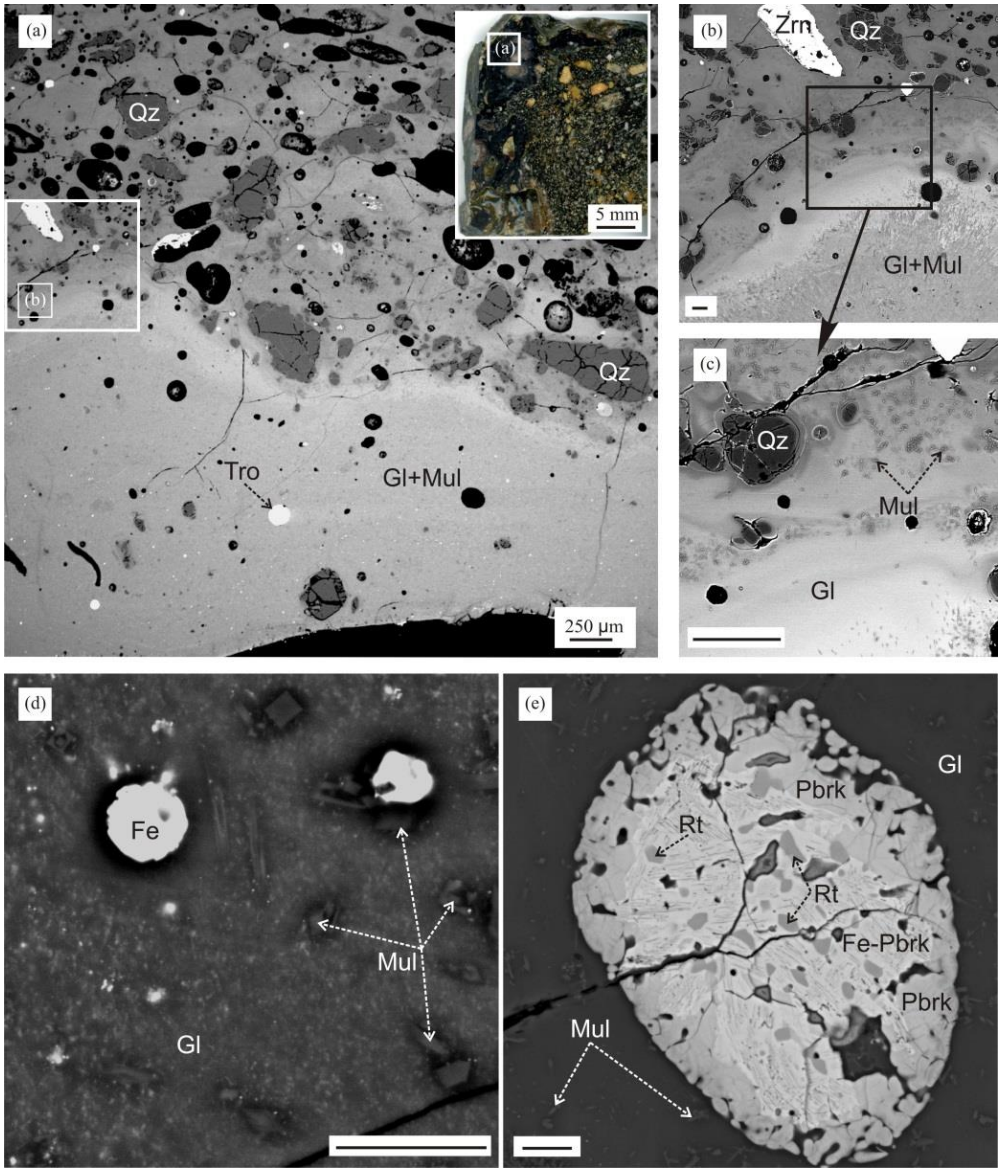

Figure 8. (a-c): Matrix fragments of paralava sample MN-1417, with enlarged vitreous zones containing grains of detrital quartz, zircon, troilite spherules, and newly formed mullite; (d): vitreous zone with Fe^0 spherules, microlites and phases of mullite and Fe-mullite; (e): grain of ferropseudobrookite–pseudobrookite with rutile inclusions. Scale bars: 100 μm for (b,c), and 10 μm for (d,e) for BSE images. Abbreviations stand for Gl = glass, Mul = mullite, Fe = metallic iron, Qz = quartz, Pbrk = pseudobrookite, Fe-Pbrk = ferropseudobrookite, Rt = rutile.

 doi:10.20944/preprints202410.1443.v1

The spherules have a troilitic rim with sporadic inclusions of Fe^0 and Fe_3P phases, a middle zone of schreibersite with inclusions of Fe^0, cohenite, and steadite, and a core with a round Fe^0 globule enclosing cohenite and schreibersite (Figure 9, Table 1). Cohenite either occurs as isolated round inclusions or is enclosed together with schreibersite or Fe^0, the phases being separated by a distinct boundary. The elemental maps and EDS spectra of cohenite (Figure 10) obtained for several zoned spherules confirmed a high concentration of carbon up to 8 wt% (e.g., 6.7 wt% C in Fe_3C: Table 1, an. 9). Meanwhile, minor amounts of carbon (~2–3 wt%) and oxygen (up to 1 wt%) were found in all phases of the spherules. Schreibersite also contains up to 2 wt% Ni and 0.6–2.6 wt% Co; Fe^0 inclusions bear ≤ 2–3 wt% P. The middle zone in some spherules is composed of Ni-rich (10–20 wt% Ni) schreibersite with inclusions of kamacite (α-Fe, 5–7 wt% Ni) and taenite (α-Fe, 10–11 wt% Ni) with ≤ 1 wt% Cu, as well as Cu sulfide compositionally similar to nukundamite $Cu_2Fe_2S_4$.

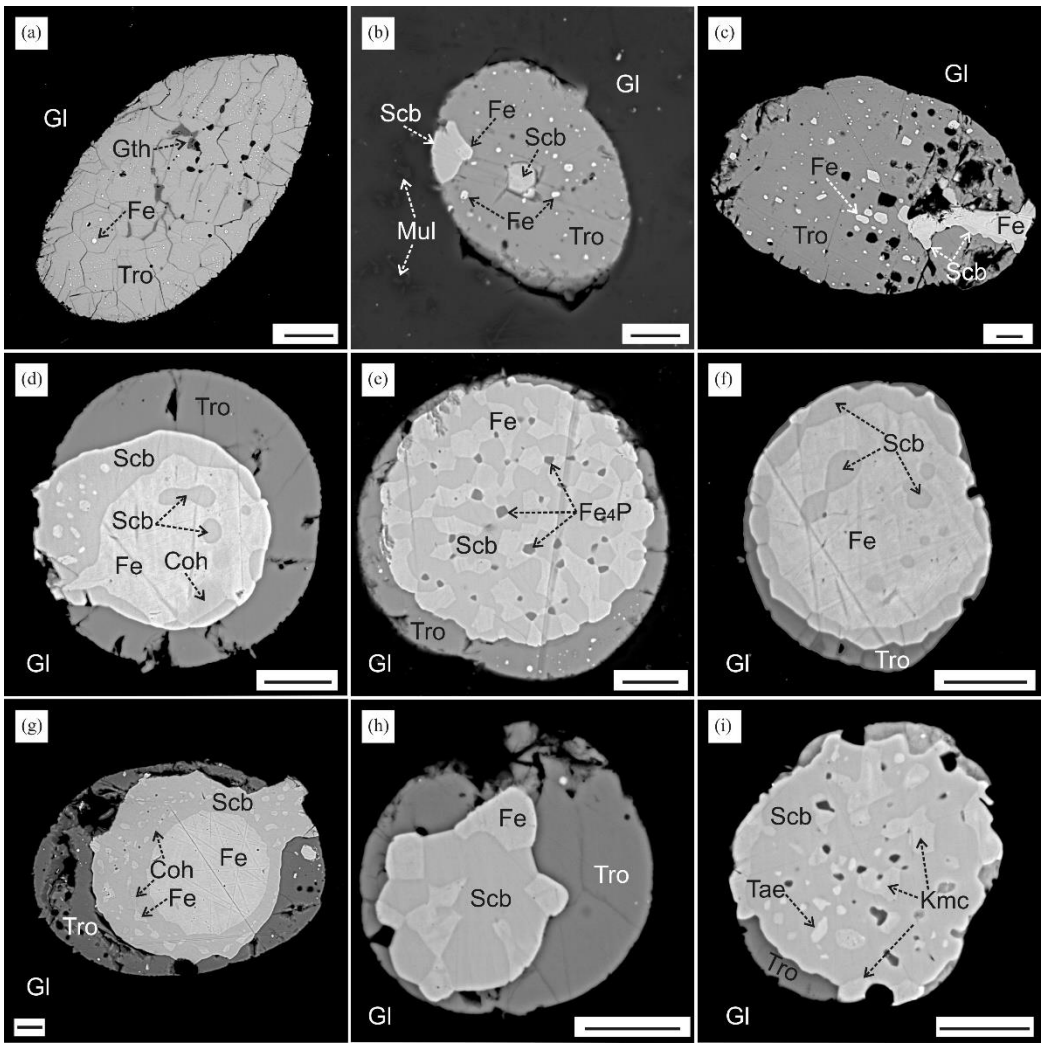

Figure 9. Isometric globules and zoned spherules in vitreous parts of paralava sample MN-1417. Scale bars: 10 μm for BSE images. Abbreviations stand for Gl = glass, Tro = troilite, Scb = schreibersite, Fe_4P = steadite, Coh = cohenite, Fe = metallic Fe, Kmc = kamacite, Tae = taenite, Gth = goethite.

 doi:10.20944/preprints202410.1443.v1

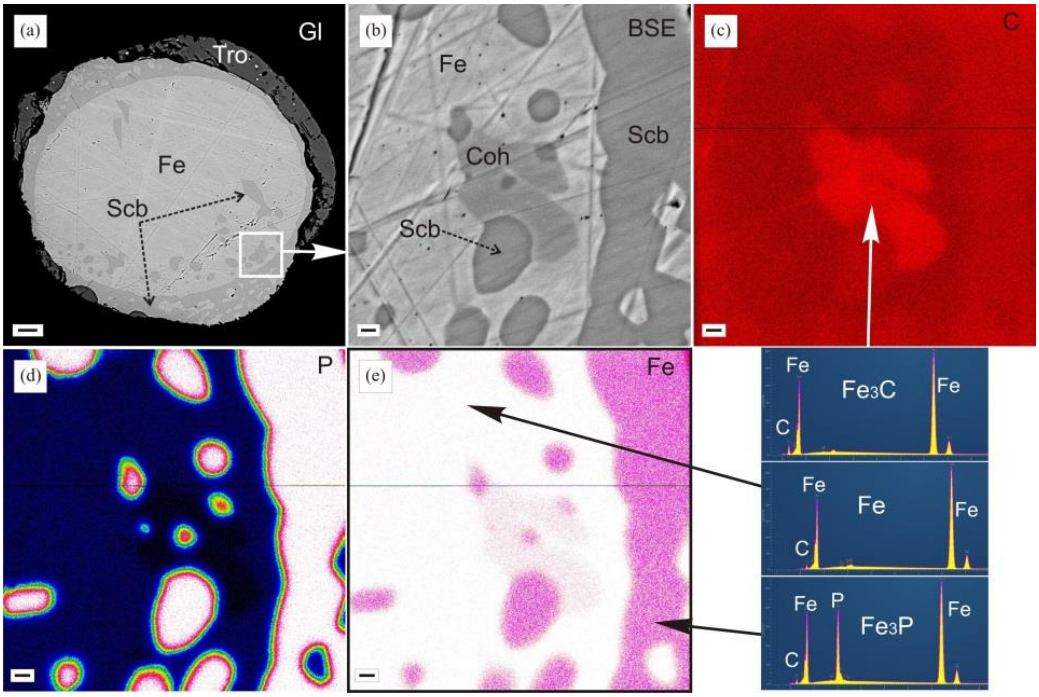

Figure 10. Zoned spherule in sample MN-1417 with schreibersite and cohenite. Scale bars: 10 μm in panel (a) and 1 μm in panels (b-e); (c,d,e): discrete color images for elements: carbon (c), phosphorus (d), iron (e); (f): EDS spectra for Fe_3C, α-Fe, and Fe_3P. Abbreviations stand for Gl = glass, Tro = troilite, Scb = schreibersite, Coh = cohenite, Fe = metallic iron.

Sample MN-1420 of melilite–nepheline paralava bears disseminated Fe^0, fine round inclusions consisting of schreibersite, Fe^0, and troilite (Figure 11) in the core of elongate basic plagioclase grains, as well as inclusions of pyrrhotite (or troilite) and perovskite intergrown with a Fe-Mn sulfide corresponding to a Fe-dominant analogue of ninengerite (Mg,Fe)S (Figure 11, Table 1, an. 5). The paralava also hosts pelitic xenoliths (mudstone baked to vitreous clinker) composed of K-rich aluminosilicate glass which encloses < 2 μm grains of cristobalite, indialite, mullite, and relatively coarse (20–40 μm) isometric cordierites. The latter sometimes have euhedral contours and, in turn, host submicrometer cristobalite and mullite inclusions. Besides these phases, the glass bears spherules of troilite, Fe^0, and < 1 to 5 μm round two-phase inclusions of Fe^0 + Fe_3P or FeS + Fe_3P.

Another sample MN-1412 of melilite–nepheline paralava contains up to 100 μm spherules of Fe^0, intergrown Fe^0 and troilite, and Fe^0 inclusions in troilite (Figure 12a-d). Many phenocrysts of plagioclase enclose ≤ 5 μm troilite ± Fe_3P, troilite + taenite (Ni-rich α-Fe, 18–21 wt% Ni, Table 1, an. 8), and sporadic Fe_2P inclusions in the core (Figure 12e-g). Some coarse plagioclase phenocrysts locally contain spinel microlites coexisting with the Fe_2P phase (Figure 12h). Iron phosphides in some inclusions bear 0.4–1.1 wt% Ni and ≤ 0.8 wt% Co. Interstitial troilite sometimes enclose Cu sulfide inclusions and veinlets correspond to the cubanite $CuFe_2S_3$ (Figure 12i, Table 1, an. 4).

Sample MN-1406 of plagioclase–orthopyroxene paralava encloses xenoliths of vitreous clinker derived from mudstone, with numerous acicular microlites of mullite, orthorhombic pyroxene (enstatite–ferrosilite), and euhedral cordierite-sekaninaite microlites (Figure 13). Glass in the xenoliths hosts small spherules of troilite, one with a round zone of schreibersite and Fe^0 and some with Fe^0 inclusions and a discontinuous chalcopyrite rim (Figure 13d-f). The spherules also enclose submicrometer particles of intergrown non-identified sulfides Cu along the spherule-glass boundaries. The sulfides have large ranges of Cu (50–70 wt%), Fe, and S, and some approach bornite compositions.

 doi:10.20944/preprints202410.1443.v1

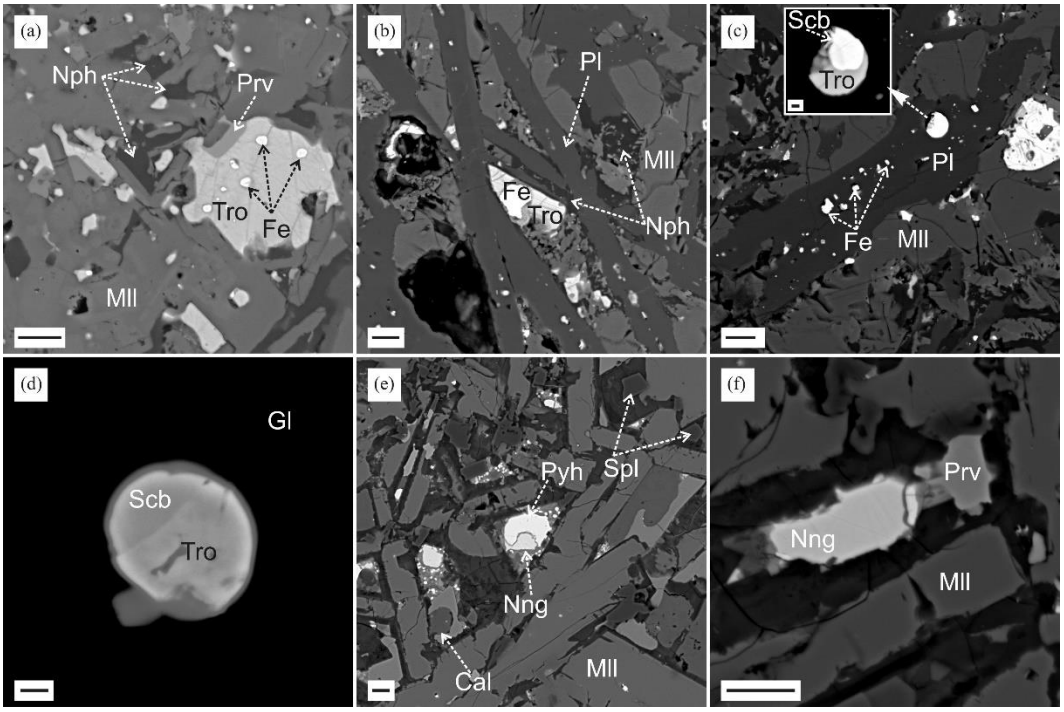

Figure 11. Matrix fragments of melilite–nepheline paralava sample MN-1420. Scale bars: 10 μm in panels (a-c,e,f) and 1 μm in panel (d) for BSE images. Abbreviations stand for Nph = Na-Ca nepheline (davidsmithite), Mll = melilite, Pl = plagioclase, Pyh = pyrrhotite, Tro = troilite, Fe = metallic Fe, Gl = glass, Spl = spinel, Prv = perovskite, Cal = calcite, Nng = ninengerite (Mg,Fe)S.

 doi:10.20944/preprints202410.1443.v1

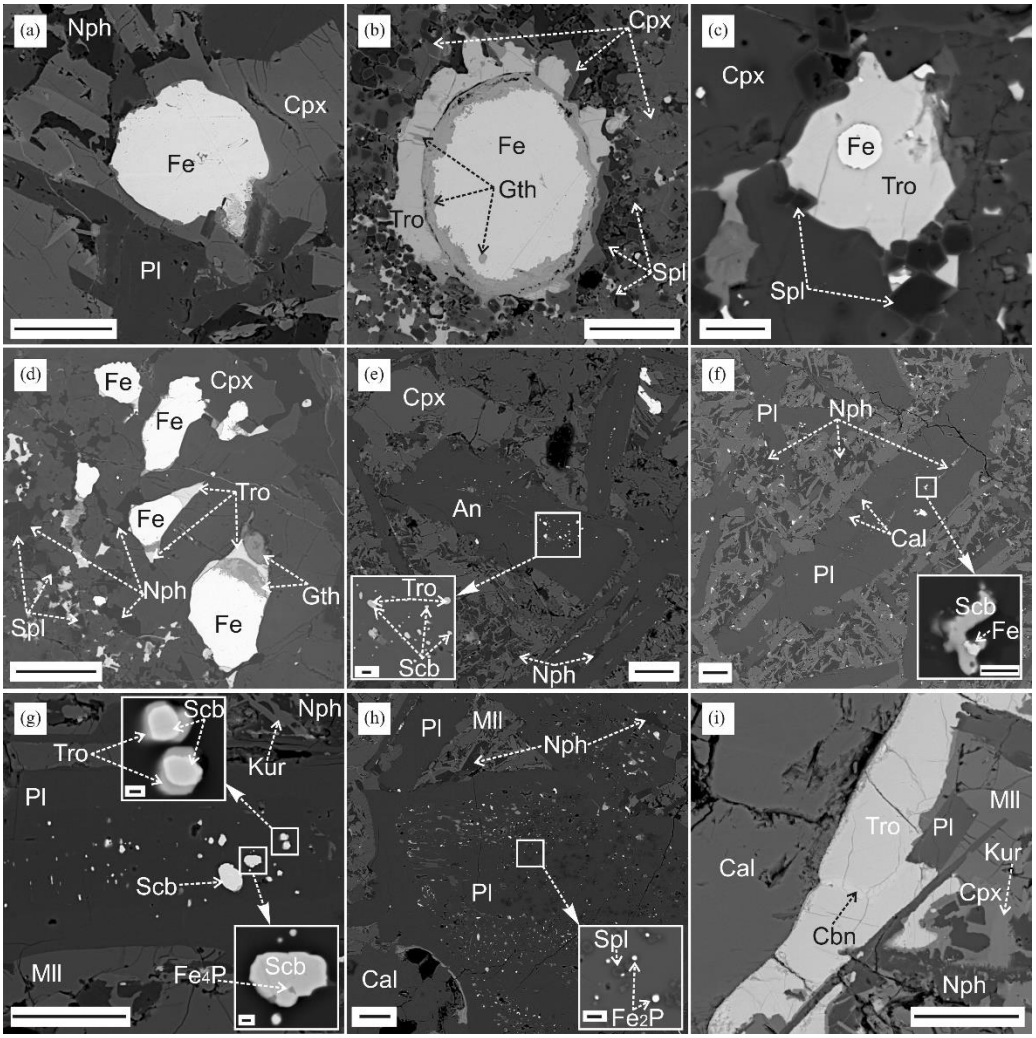

Figure 12. Matrix fragments of melilite-nepheline paralava sample MN-1412. Scale bars: 50 μm for all BSE images, 5 μm for insets in panels (e,f,h), and 1 μm for inset in panel (g). Abbreviations stand for Nph = Ca-rich nepheline (davidsmithite), Mll = melilite, Pl = plagioclase, Cpx = clinopyroxene, Kur = kuratite, Spl = spinel, Tro = troilite, Fe = metallic Fe, Gth = goethite, Scb = schreibersite, Fe_2P = barringerite or allobogdanite, Fe_4P = steadite, Cub = cubanite $CuFe_2S_3$, Cal = calcite.

 doi:10.20944/preprints202410.1443.v1

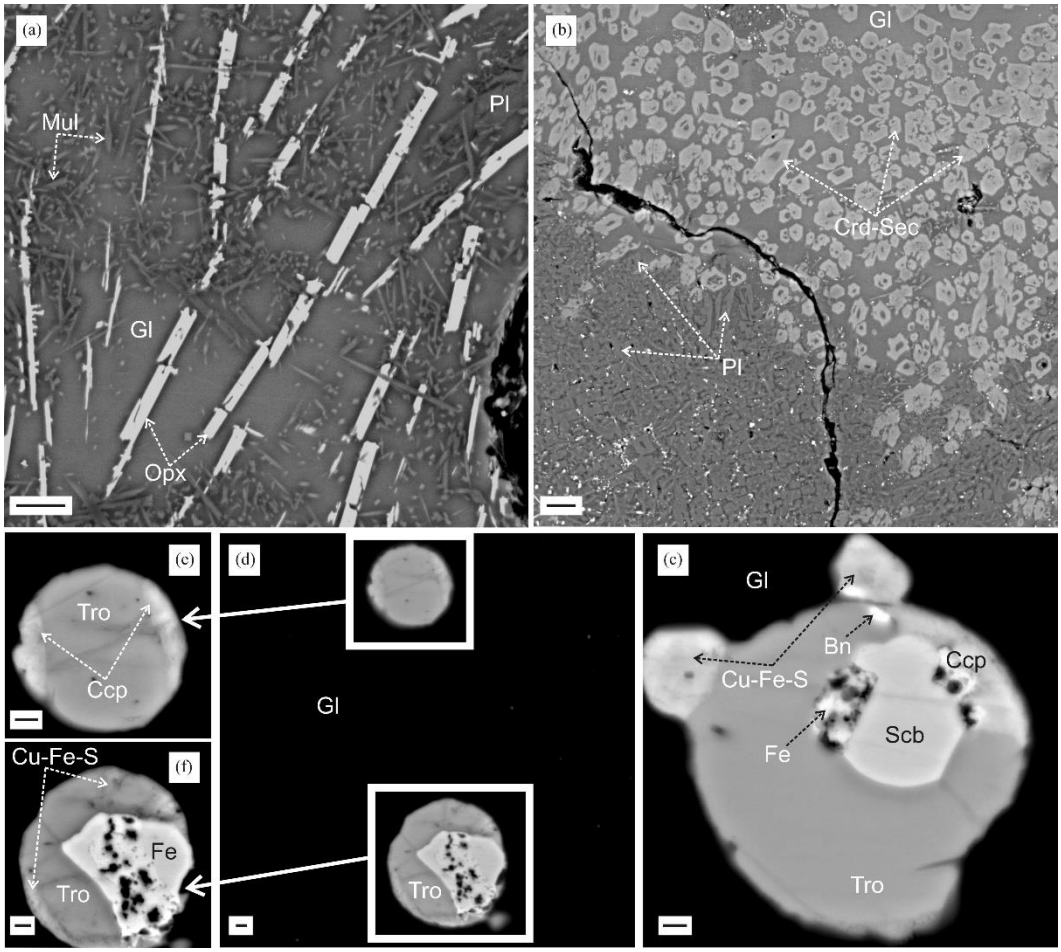

Figure 13. Matrix fragments of plagioclase–orthopyroxene paralava sample MN-1406. Scale bars: 10 μm in panels (a, b) and 1 μm in panels (c-f) for BSE images. Abbreviations stand for Gl = glass, Opx = orthopyroxene, Pl = plagioclase, Crd-Sec = cordierite-sekaninaite, Tro = troilite, Fe = metallic Fe, Scb = schreibersite, Std = steadite, Bn = bornite (?), Ccp = chalcopyrite, Cu-Fe-S = non-identified Cu-Fe sulfides.

4. Discussion

4.1. Formation of Melilite-Nepheline Paralava: Conditions and Processes

Earlier we [3,6] suggested a qualitative petrological model explaining the formation of the Khamaryn–Khyral–Khiid melilite–nepheline paralava and carbonate melt by melting of marly limestone. The model implied crystallization of a gehlenite + Al-clinopyroxene assemblage in marly limestone layers during high-temperature low-pressure combustion metamorphism of sediments as a result of wild underground coal fires. The thermal alteration occurred at relatively high partial pressure of CO_2 in unique *P-T* conditions without decomposition of calcite into CaO and CO_2 [6].

Melting of K-Na feldspar in the silicate (pelitic) component of marly limestone occurred at $T > 1100$ °C and $P_{CO2} > 40$ bar, while calcite, gehlenite, Al-clinopyroxene, and other refractory minerals melted incongruently at $T > 1250$ °C, $P_{CO2} > 40$ bar. The melts comprised immiscible carbonate (non-stoichiometric $CaCO_3$ + CaO or stoichiometric calcitic) and several compositionally diverse silicate melts [6]. Coalescence of melts derived from silicate minerals led to the formation of a liquid undersaturated with respect to Si and enriched in Ca which became the parent melt of melilite–nepheline paralava. The paralava matrix locally preserves gehlenite grains with rims of newly formed ferroan åkermanite–alumoåkermanite and remnant marly limestone xenoliths composed of

 doi:10.20944/preprints202410.1443.v1

gehlenite, monticellite–kirschsteinite, forsterite, perovskite, calcite, sulfates, and other rare phases, in different relative percentages, these assemblages being exotic for melilite–nepheline paralava [2,3,6].

As indicated by petrography and SEM-EDS data, the sequence of crystallization from the parent melts of melilite–nepheline paralava was as follows: (1) spinel-group microlites with large ranges of Fe^{2+}, Fe^{3+}, Al, and Mg, as well as phosphide Fe_2P in some paralava varieties [3]; (2) a phenocryst assemblage of bytownite–labradorite, ferroan åkermanite–alumoåkermanite, and Al-clinopyroxene (diopside with a high percentage of the kushiroite end-member); (3) interstitial phases of olivine (Ca-bearing fayalite, kirschsteinite), K-Ba feldspar (celsian, hyalophane), rhönite–kuratite series, fluorapatite, spinel, pyrrhotite or troilite, Na-K nepheline (Nyalga complex) or Na-Ca nepheline (davidsmithite, Khamaryn–Khyral–Khiid complex), kalsilite, barite, and other minerals, including very rare ones [2,3,5].

The data on mineral assemblages in the melilite–nepheline paralava of the two CM complexes in Mongolia allowed estimating the crystallization temperatures of the rhönite–kuratite series (~1100 °C) and the temperature range for exsolution of Fe-Ca olivine into Ca-bearing fayalite and kirschsteinite (1000–800 °C) at oxygen fugacity varying between the IW and FMQ (Fayalite–Magnetite–Quartz) buffers [2,3].

The samples of melilite–nepheline paralava (MN-1412 and MN-1420) enclose iron phosphides: Fe_2P + Fe_3P in the early growth zone of anorthite–bytownite phenocrysts and schreibersite in aluminosilicate glass produced by vitrification of melt during the melting of clinker xenoliths in the paralava of samples MN-1420 and MN-1412 (Figures 11 and 12). The clinker xenoliths in sample MN-1420 contain mullite, indialite, and cristobalite due to a high melt temperature which possibly reached the stability field of β-cristobalite at $T > 1470$ °C [5].

The findings of reduced mineral assemblages with metallic iron, iron phosphides, magnesiowüstite–ferropericlase, and wüstite provide direct evidence of high-temperature extreme redox conditions at a certain crystallization stage of silica-undersaturated Ca-rich mafic melts (parent to melilite–nepheline paralavas) and vitrification of felsic aluminosilicate melts in clinker. Below we discuss possible processes and conditions responsible for the presence of reduced assemblages in the studied CM rocks.

4.2. (Mg,Fe)O, MgO–FeO Solid Solution

The ferropericlase–magnesiowüstite solid solution is an essential component of the Earth's lower mantle [18] where phase change of ringwoodite $(Mg,Fe)_2SiO_4$ (silicate spinel) at high pressure leads to the formation of perovskite $(Mg,Fe)SiO_3$ and ferropericlase (Mg,Fe)O. The unusually large range of iron content in ferropericlase (Mg# 12–93) from diamond inclusions is due to its origin at mantle depths of 410 to 660 km [19]. Considering that periclase with < 5 wt% FeO is of rare occurrence in the Earth's crust and proceeding from analysis of crystal structure, the solid solution between MgO and FeO is expected to be unstable in the low-pressure crustal conditions [20].

The Mg-Fe oxide with variable FeO and MgO contents appears in the Raman spectra as a crystalline compound (Figure 6b) within the joint between wüstite and periclase. The presence of the exotic magnesiowüstite–ferropericlase + spinel $(Mg,Fe)Al_2O_4$ + forsterite assemblage (Figure 7e-g) in melilite–nepheline paralava hardly can be attributed to high-pressure formation conditions of mantle rocks but rather must result from melting of carbonate-silicate sedimentary protoliths. According to our qualitative petrological model [6], melilite–nepheline paralava was produced by incongruent melting of marly limestone. This prediction agrees with the $CaO–CaCO_3$ phase diagram in the low-pressure region implying melting of calcite [21], as well as with the abundance of paralava-hosted calcite melt inclusions in mineral phenocrysts and sedimentary xenoliths composed of spinel, forsterite, monticellite, perovskite, calcite, and other phases [2,3]. The Nyalga melilite–nepheline paralava likewise bears remnant sedimentary xenoliths consisting of magnesioferrite, larnite, baritocelestine, sulfates, gehlenite, perovskite, fayalite, and periclase with 10–15 wt% FeO. The parts of paralava matrix with magnesiowüstite–ferropericlase grains in association with spinel and

 doi:10.20944/preprints202410.1443.v1

forsterite (Figure 7e-g) are likewise remnants of sedimentary xenolith or ferroan sinter produced by melting of ash after coal combustion.

Published evidence from metallurgical production experience shows that Fe, Mg, and Al oxides enter many sinter and refractory materials used for lining up steel-smelting furnaces, and variations of their contents can affect notably the physical properties (melting point, viscosity, fluidity, etc.) of the lining materials. The FeO–MgO phase diagram has been well constrained experimentally and correlated with thermodynamic calculations [22–24]. Both liquid and solid oxides in the FeO–MgO system have unlimited solubility (Figure 14). In reducing conditions at atmospheric pressure, the FeO–MgO–Al_2O_3 phase diagram includes regions of equilibrium between an oxide melt and the magnesiowüstite–ferropericlase and spinel (Mg,Fe)Al_2O_4 solid solutions, while the solubility in MgO is unlimited for FeO and limited for Al_2O_3 (Figure 14).

The FeO–MgO and FeO–MgO–Al_2O_3 phase diagrams show that magnesiowüstite–ferropericlase and spinel in melilite–nepheline paralava sample MN-1133 may have melted (or crystallized) in a reducing environment at 1800–1600 °C. The temperature of underground coal fires not necessarily was that high though, because the conditions and processes during low-pressure melting of sediments have multiple controls, such as compositions of coal and sedimentary protoliths, fluid regime, combustion kinetics, etc. Meanwhile, the mineral assemblage of magnesiowüstite–ferropericlase + spinel + forsterite was formed at low oxygen fugacity and at temperatures higher than for any other known paralava assemblage, possibly, at the fire focus. Note also that magnesiowüstite–ferropericlase grains became replaced by magnesioferrite while the paralava was cooling down or weathered in an oxidizing environment (Figure 7e-g).

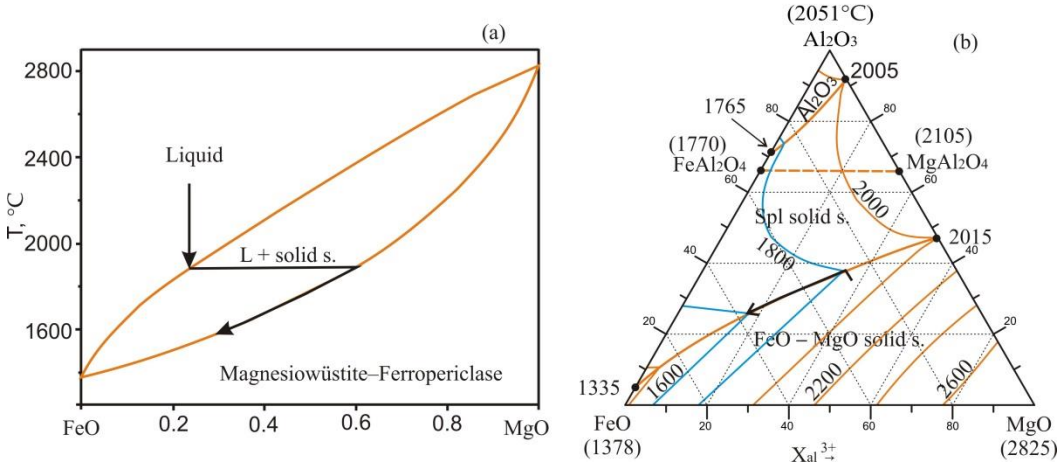

Figure 14. FeO–MgO and FeO–MgO–Al_2O_3 phase diagrams according to thermodynamic modeling Samoilova and Markovets [22] with reference to experimental data [Schenck and Pfaff; Scheel [23,24]. Lines with arrows are crystallization paths of Mg–Fe and Mg–Fe–Al melts which produced magnesiowüstite–ferropericlase with Mg# 0.6–0.3 in the 1800–1600 °C temperature range (a) and solid solution of spinel cotectic assemblage (Fe,Mg)Al_2O_4 + MgO–FeO (b).

4.3. Troilite with Inclusion of Metallic Iron and Pyrrhotite

Melilite–nepheline paralava and vitreous clinker fragments often contain globules or spherules of iron monosulfide (pyrrhotite or less often troilite) with inclusions of metallic iron. High-temperature iron monosulfide crystallized from droplets of Fe–S melt occurring in the silicate melt of paralava.

As follows from the Fe–S phase diagram (Figure 3), pyrrhotite grains (free from Fe^0 inclusions) may have crystallized from an Fe–S melt with mole fraction 0.54–0.50 S which existed at temperatures above 1100 °C. A melt with a lower S fraction (0.50–0.43) can precipitate pyrrhotite upon cooling below 1190 °C while γ-Fe forms at 988 °C at the eutectic point. That was probably the case for a large pyrrhotite grain from sample MN-1287 which acquired symplectitic zones with inclusions of wüstite

 doi:10.20944/preprints202410.1443.v1

and magnetite (Figure 5). The two minerals probably resulted from oxidation of metallic Fe originally present in the inclusions, first to wüstite and then partly to magnetite at increasing oxygen fugacity (Figure 5c,e). Upon cooling to 140 °C, pyrrhotite converted into the stable phase of troilite which became partly replaced by marcasite along cracks during weathering (Figures 3 and 5).

Judging by the texture of the paralava and the phase diagram (Figure 3), the troilite globules with Fe^0 inclusions crystallized from a Fe–S melt with a low mole fraction of S (< 0.43). The crystallization of iron was followed by that of high-temperature pyrrhotite at 988 °C, which then converted to troilite upon cooling at 140 °C.

4.4. Mineral Assemblages with Iron Phosphides

Iron phosphides (± Ni-bearing) are especially common to mineral assemblages of meteorites but are of rare terrestrial occurrence restricted to CM rocks and some volcanics, e.g., in Disko Island, Greenland [25,26]. Recently structural features of iron phosphides (barringerite, schreibersite, murashkoite FeP, zuktamrurite FeP_2) and Ni–Fe–Mo–Cr phosphides (nickelphosphide $(Ni,P)_3P$, allobogdanite $(Fe,Ni)_2P$, orishchinite Ni_2P, transjordanite Ni_2P, negevite NiP_2, halamishite Ni_5P_4, nazarovite $Ni_{12}P_5$, andreyivanovite FeCrP, nickolayite FeMoP, polekhovskyte $MoNiP_2$) have been discovered in the Hatrurim Formation (Israel and Ohman) and documented in more or less detail [27–37]. However, the Hatrurim phosphide-bearing CM rocks remain very poorly studied in terms of petrology.

In this respect, it is especially interesting to reconstruct the crystallization conditions of iron phosphides (schreibersite and Fe_2P) found in melilite–nepheline paralava samples MN-1420 and MN-1412 (Figures 11 and 12), as well as in vitreous zones of clinker xenoliths from paralava samples MN-1406 and MN-1417 (Figures 8–10 and 13). Note that allobogdanite was previously considered as a high-pressure orthorhombic polymorph $(Fe,Ni)_2P$ [28,38] before it was found out that Ni-free Fe_2P also crystallized in a orthorhombic structure at ambient pressure [39] and the allobogdanite to hexagonal barringerite conversion occurred at ~600 °C [40].

The possible conditions and sequence of crystallization of iron phosphides (Fe_3P and Fe_2P) from inclusions in the core (early growth zone) of many basic plagioclase phenocrysts from melilite-nepheline paralava samples MN-1420 and MN-1412 can be estimated using the Fe–P phase diagram which has been well studied topologically (Figure 15). Plagioclase phenocrysts mostly bear schreibersite, as isolated inclusions or intergrown with troilite (crystallized drops) or Fe^0, while Fe_2P occurs in a few inclusions (Figures 11c and 12e-h).

According to the Fe–P phase diagram at ambient pressure, the Fe–P melt containing 14–22 wt% P first precipitates the Fe_2P phase at $T < 1370$ °C, then Fe_3P forms by the peritectic reaction Fe–P melt + Fe_2P at 1165 °C and exists till the equilibrium eutectic phase of Fe_4P (steadite = α-Fe + Fe_3P) crystallizes at 1048 °C (Figure 15).

Thus, the cooling parent melt of paralava apparently captured different inclusions at decreasing temperatures (Figure 15, Paths I and II): Fe_2P at 1370–1165 °C, sometimes together with Al-spinel microlites occurring in the core of plagioclase phenocrysts from paralava samples MN-1420 (Figure 11c) and MN-1412 (Figure 12e-h), and Fe_3P at 1165 °C to 1048 °C. Sporadic inclusions of Fe_4P (steadite) are apparently a eutectic mixture of submicrometer Fe^0 and Fe_3P phases stable below 1048 °C, which are undetectable by SEM-EDS because of small size.

 doi:10.20944/preprints202410.1443.v1

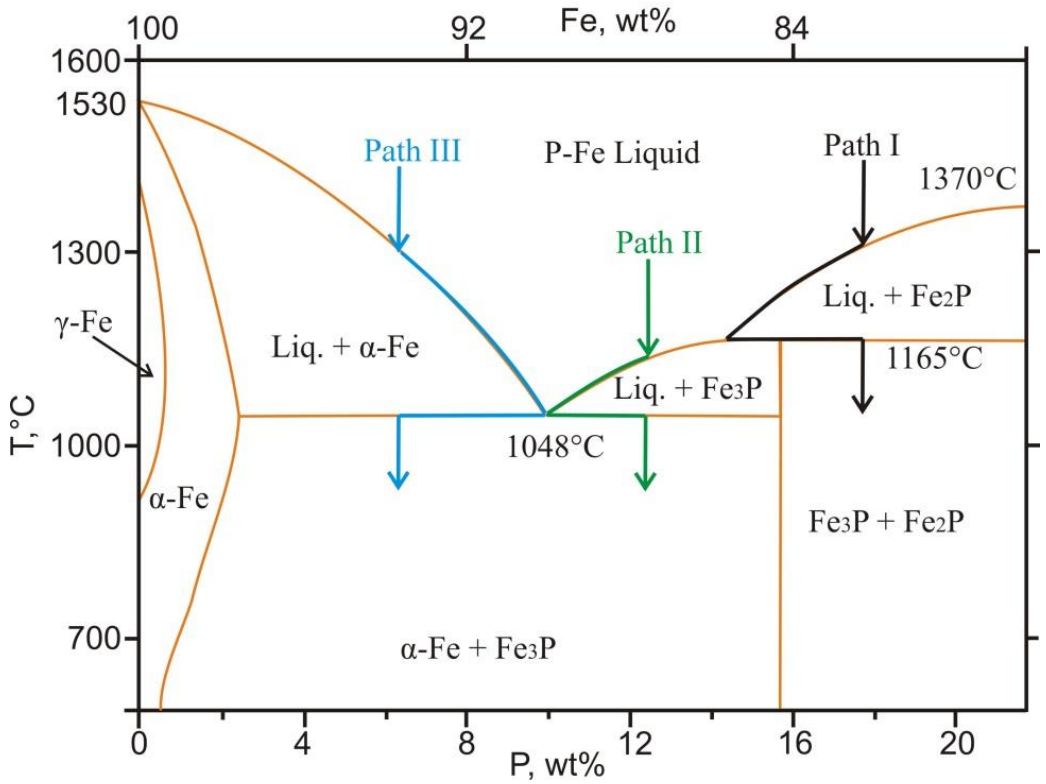

Figure 15. Simplified Fe–P phase diagram at 1 bar, after Miettinen and Vassilev [41]. Arrows are three crystallization paths of a Fe–P melt with different P contents. Path I: 1370 °C to 1165 °C, formation of Fe_2P and then $Fe_2P + Fe_3P$; Path II: 1165 °C to 1048 °C, formation of Fe_3P and then α-Fe + Fe_3P; Path III: 1530 °C to 1048 °C, formation of α-Fe and then α-Fe + Fe_3P.

Phase relationships are more complex in zoned spherules consisting of troilite, Fe^0 or kamacite, taneite, schreibersite ± (steadite and cohenite) found in melt rock sample MN-1417 (Figures 9 and 10). The crystallization conditions and sequence can be inferred from their texture using the Fe–S, Fe–P–C, and Fe–P–S phase diagrams.

The possible formation conditions of troilite phenocrysts and spherules with inclusions of Fe^0 in the vitreous zones of sample MN-1417 were estimated using the Fe–P phase diagram (Figure 15). Troilite in other coarser zoned spherules commonly rims the phases of Fe^0, schreibersite ± (cohenite and steadite) present in different volume percentages (Figure 9).

Different phases in the zoned spherules may have followed two possible models of crystallization from a silicate melt which contained either (1) droplets of a homogeneous Fe–S–P–C melt decomposed into immiscible Fe–S and Fe–P–C liquids upon cooling or (2) droplets of Fe–P–S–C, Fe–S, Fe–P–C, and Fe–P–S–C liquids coalesced partly into larger homogeneous drops with different ratios of S, Fe, P and C or into drops consisting of two immiscible melts. Model 2 appears more realistic because inclusions, globules and spherules show large variations of volume phase relations among troilite, Fe^0, Fe_3P, and Fe_3C.

The Fe–S–P phase diagram was studied previously [42–44] at oxygen fugacity corresponding to the IW and QFI (Quartz–Fayalite–Iron) buffers equilibria. It comprised fields of a homogeneous Fe–S–P melt and a region of immiscibility between a Fe–S (sulfide) and Fe–P (phosphide) melts (Figure 16).

Preprints.org (www.preprints.org) | NOT PEER-REVIEWED | Posted: 18 October 2024 doi:10.20944/preprints202410.1443.v1

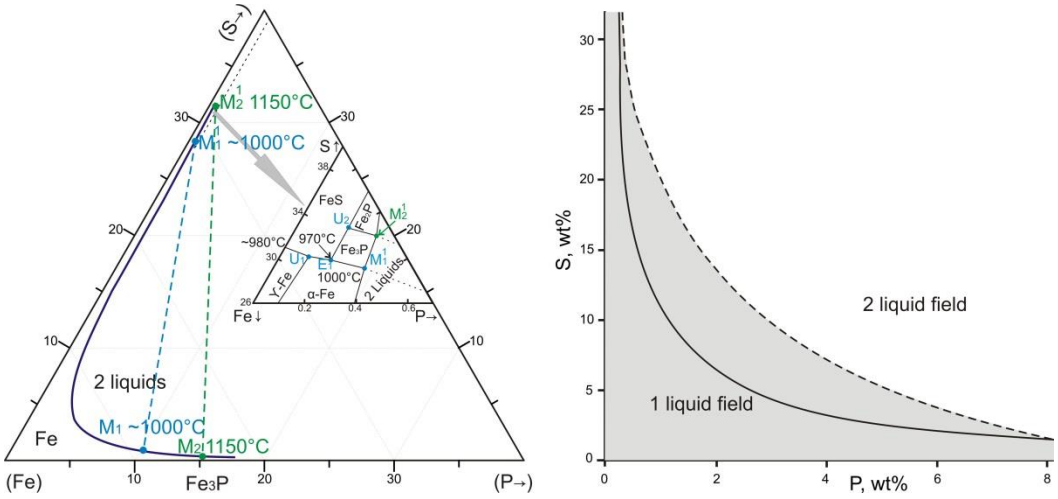

Figure 16. (a): Fe-rich corner of the Fe–P–S diagram, after Jones and Drake [42]. Solid line shows the location of the two-liquids solvus. M_1 and M_1^1 are invariant points (shown connected by dashed lines) where next condensed phases stably coexist: M_1 and M_1^1 (Fe, Fe_3P, two liquids) at ~1000 °C; E_1 (Fe, Fe_3P, FeS) at 970 °C; M_2 and M_2^1 (Fe_3P, Fe_2P, two liquids) at 1150 °C; U_2 (Fe_3P, Fe_2P, FeS); (b): Fe–P–S phase diagram in the P–S section. Solid line is a boundary between the miscibility domains of liquids, after Raghavan [43]. Dashed line limits the field of a homogeneous Fe–P–S melt at 1350°C (IW buffer) and the field of two (phosphide and sulfide) liquids at 1250°C (IW and QFI buffers), after Chabot and Drake [44].

As follows from the phase diagram and published data [42–44], the homogeneous Fe–S–P melt in the spherules could exist at ~1350 °C and decomposed into immiscible Fe–P and Fe–S melts in the ~1350–1250°C range. In our case, the Fe–S–P melt contained minor amounts of carbon which complicated the relationships of crystallized phases and could shift the phase change temperatures.

After the homogeneous melt had decomposed upon cooling, the spherules accommodated two immiscible liquids: a dense Fe–P–C melt in the core and a less dense Fe–S melt in the rim. The phases crystallized from the two melts were, respectively, high-temperature pyrrhotitic (4.61 g/cm^3 on average) and several higher-density phases: Fe^0 (7.87 g/cm^3), Fe_3P (6.74 g/cm^3) ± (Fe_4P + Fe_3C). In the course of further cooling, the melts evolved in accordance with the Fe–S and Fe–P–C phase relations. Metallic iron was the first to crystallize, judging by the texture of spherules (Figure 9), which is possible in a iron-saturated Fe–P–C melt with different relative contents of P and C above the eutectic point at T > 952 °C, as one may infer from the place of the liquidus surface in the Fe–P–C system (Figure 17). Paths 1 and 2 in Figure 17 show composition changes in the Fe–P–C melt from the α-Fe (bbc) or γ-Fe (fcc) fields, with the following crystallization sequence: C-bearing α-Fe or γ-Fe → cotectic α-Fe or γ-Fe + Fe_3P → eutectic (E_T) γ-Fe + Fe_3P + Fe_3C.

In some spherules, the schreibersite zone with inclusions of Fe^0 ± Fe_3C breaks through the troilite rim (Figures 4 and 9d,g). Therefore, the Fe–P–C parent melt for this zone was liquid (mobile) after the crystallization of high-temperature pyrrhotite in the spherule rim (at T < 988 °C according to the Fe–S phase diagram, Figure 3). The texture features of the spherules are consistent with the crystallization sequence along Path 3 in the Fe–P–C phase diagram: C-bearing γ-Fe → cotectic γ-Fe + Fe_3C → eutectic (E_T) at 952 °C (Figure 17). Thus, the final crystallization stage in the zoned spherules may have occurred in the 988–952 °C range while the large drops of homogeneous Fe–P–S–C melt and immiscible Fe–S and Fe–P melts the could coexist at a temperature as high as 1350 °C (Figures 15–17).

 doi:10.20944/preprints202410.1443.v1

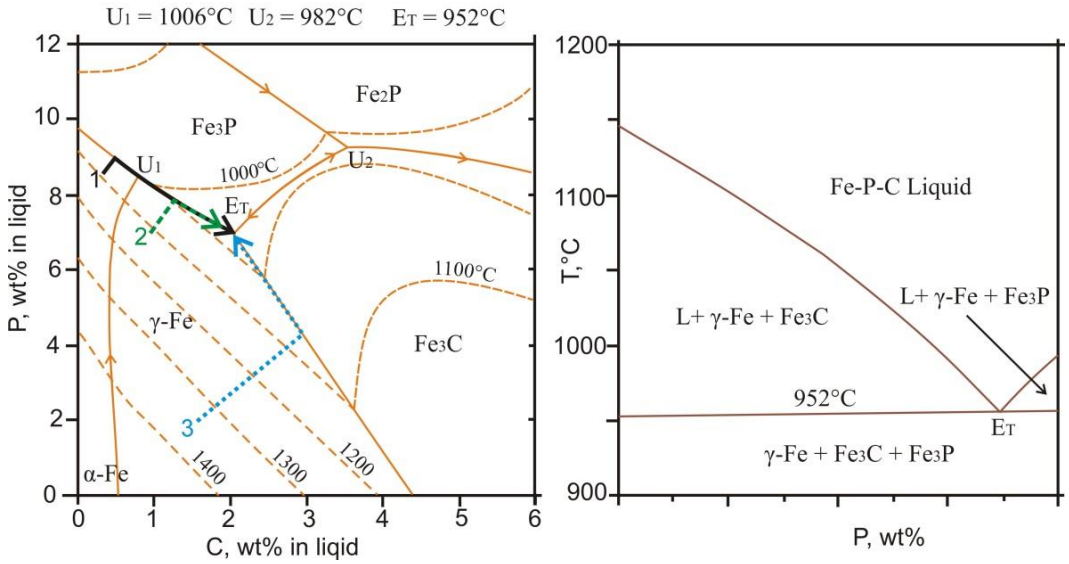

Figure 17. Liquidus surface projection of the Fe–P–C system in the Fe-rich corner (a) and vertical section along metastable reaction of Liguidus = γ-Fe (fcc) + Fe_3C (b), after thermodynamic assessment Shim et al. [45] and experimental data Schurmann [46]. 1, 2, and 3 and lines with arrows show three evolution paths of the Fe–P–C melt on the liquidus surface.

4.5. Formation Conditions of Reduced Mineral Assemblages

The findings of enclosed iron phosphides (Fe_2P, Fe_3P) and troilite ± Fe^0 in the early growth zone of plagioclase phenocrysts from melilite–nepheline paralava samples MN-1412 and MN-1420, as well as in glass from clinker xenoliths of paralava samples MN-1420 and MN-1406, together with zoned spherules composed of troilite, Fe^0, Fe_3P, and Fe_3C in sample MN-1417, indicate the presence of Fe–S, Fe–P, and Fe–P–S–C melt drops in the paralava. This melt drops were captured by growing plagioclase phenocrysts early during the formation of the mineral assemblage in the paralava matrix.

Iron phosphides and Fe^0 can co-crystallize only at oxygen fugacity below the IW buffer and, for this reason, are found together in many stony-iron and iron meteorites. In this respect, the presence of extremely reduced mineral assemblages in some rocks of the Nyalga and Khamaryn–Khural–Khiid complexes is hard to explain as they result from multi-stage thermal metamorphism and partial melting of sediments during coal combustion which requires oxygen access.

Hypothetically, some low-permeable overburden domains above underground fire foci may have undergone thermal alteration with very limited to zero air inputs, by conductive heat transferred from adjacent burning parts of coal seams. Similar processes of thermal metamorphism in extremely reducing conditions were inferred for rocks deep inside large burnt waste dumps (so-called *black blocks*) in the Chelyabinsk coal basin [47]. The fluid (gas) regime in these zones, at impeded access of atmospheric oxygen, excess of atomic carbon, and lack of water, was controlled by the CCO buffer.

The probable redox evolution during melting of marly limestone, crystallization and subsequent cooling of melilite–nepheline paralava is presented in the T–LgP_{O2} diagram (Figure 18) based on estimated crystallization temperatures of reduced mineral assemblages.

The highest-temperature mineral assemblage of magnesiowüstite–ferropericlase, Mg-Fe spinel, and forsterite in remnant sinter from the paralava matrix of sample MN-1133 (Figure 7 e-g) was formed at oxygen fugacity between the WM and IW buffers, while the T > 1500–1600 °C melting temperatures of the sinter based on the FeO–MgO and FeO–MgO–Al_2O_3 phase diagrams (Figure 14) can be overestimated (see above).

At ~1350 °C, large zoned spherules may have accommodated a homogeneous Fe–P–S–C melt (Figures 9, 10 and 16) which produced zones of troilite, schreibersite and Fe^0 ± (Fe_3C + Fe_4P). High-temperature phosphide Fe_2P in plagioclase phenocrysts may have crystallized at temperatures

 doi:10.20944/preprints202410.1443.v1

between 1370 °C and 1165 °C (Figure 15) and at oxygen fugacity far below the IW buffer ($\Delta\log fO_2$ (IW) – 6 according to [25,26]), in extremely reducing conditions probably controlled by the CCO buffer equilibrium.

Schreibersite from plagioclase phenocrysts, as well as the $Fe_3P + Fe^0 + Fe_3C$ assemblage in zoned spherules, crystallized between 1165 °C and 952 °C, at fO_2 about the CCO buffer (Figures 15, 17 and 18). The matrix of melilite–nepheline paralava samples MN-1133, MN-1287, MN-1420, MN-1412, and MN-1406 had been completely formed before the system cooled down to 850–800 °C, or the minimum crystallization temperature for the Fe-Ca olivine solid solution [2]. At the same time, mineral assemblages free from Fe^0 and iron phosphides crystallized at a higher oxygen fugacity about the FMQ buffer [1,2].

The crystallization temperature of iron monosulfide (high-temperature pyrrhotite) in large grains and in eutectic symplectites with wüstite–magnetite inclusions (Figures 5 and 7), which crystallized from Fe^0, varied from < 1190 °C to 988 °C (Figure 3). As the crystallized paralava was cooling down, metallic iron in monosulfide grains self-oxidized to wüstite and magnetite (Figures 5 and 7) because the affinity of iron to oxygen increases faster than that of carbon. The equilibria overlap at ~720 °C (CCO–IW and CCO–IM) and at ~550 °C (IW–MW and IW–IM) (Figure 18). Meanwhile, the self-oxidation of Fe^0 to wüstite (sample MN-1133, Figure 7) and wüstite to magnetite (samples MN-1133 and MN-1287, Figures 5 and 7) in iron monosulfide grains remained locally incomplete as paralava cooled down relatively rapidly. Furthermore, Fe^0, wüstite, and magnetite coexist at < 550 °C in a small $Lg P_{O2}$ region confined by the WM, IW, and IM buffers equilibria. Upon further cooling to < 140 °C, iron monosulfide underwent solid-state transition to troilite (Figure 3), while magnetite and troilite became partly replaced by goethite and marcasite, respectively, at lower temperatures and/or during weathering (Figures 5 and 7).

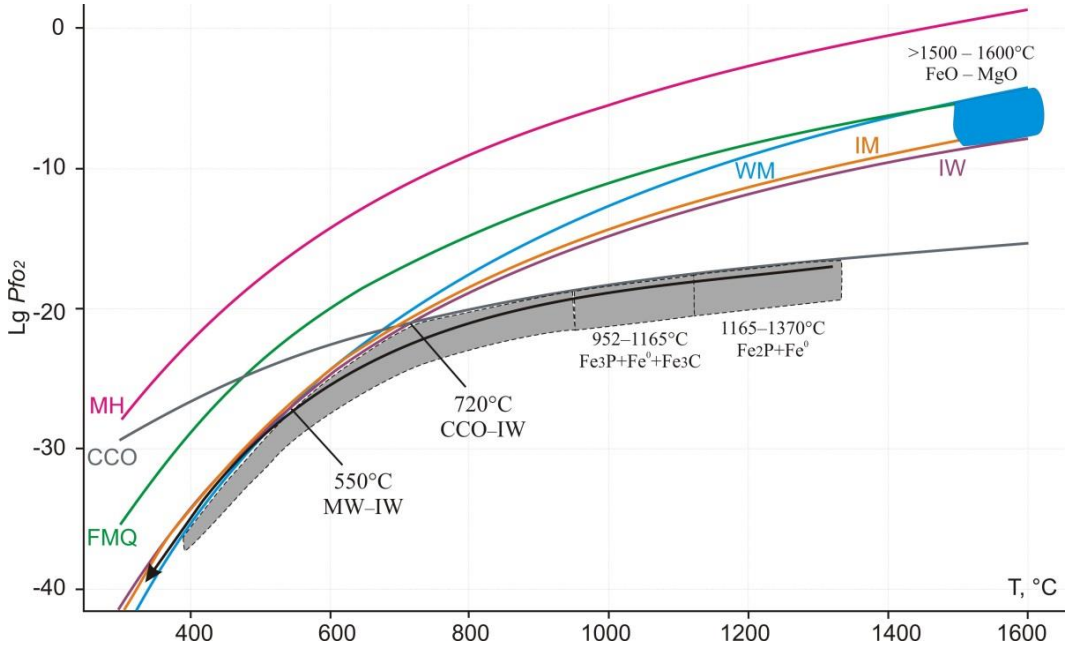

Figure 18. Redox evolution (heavy arrow) during crystallization of magnesiowüstite–ferropericlase, iron phosphides (Fe_2P, Fe_3P), metallic iron, cohenite, wüstite, and magnetite (see text for explanation). Colored fields refer to hypothetical crystallization conditions of reducing mineral assemblages, in T–$Lg P_{O2}$ coordinates. CCO, IW, IM, WM, FMQ, and MH are buffer equilibria. Equilibria intersections are at 720 °C for CCO and IW and at 550 °C for IW and WM.

5. Conclusions

Reducing mineral assemblages of $FeS + Fe^0 + Fe_2P + Fe_3P$ and $FeS + Fe^0 + Fe_3P + Fe_3C + Fe_4P$ were studied comprehensively in several samples of melilite–nepheline paralava and other thermally

 doi:10.20944/preprints202410.1443.v1

altered and partly melted rocks from the Naylga and Khamaryn–Khyral–Khiid combustion metamorphic complexes in Mongolia.

The paralava samples include matrix fragment composed of magnesiowüstite–ferropericlase, spinel $(Mg,Fe)Al_2O_4$, and forsterite. As inferred from the MgO–FeO and MgO–FeO–Al_2O_3 phase diagrams, this mineral assemblage has the highest crystallization temperatures and may represent Fe-rich sinter produced by melting of coal combustion ash.

The crystallization temperature were also inferred from the Fe–S phase diagram for paralava-hosted iron monosulfide (high-temperature pyrrhotite) with Fe^0 inclusions which converted to the stable phase of troilite by solid-state transformation at 140 °C.

The Fe–P phase diagram was used to reconstruct the crystallization conditions of iron phosphides Fe_2P, Fe_3P, and Fe_4P in inclusions from the early growth zone of plagioclase phenocrysts in the melilite–nepheline paralava matrix: < 1370–1165 °C, 1165–1048 °C, and < 1048 °C, respectively.

The analyzed samples enclose large zoned spherules consisting of troilite, Fe^0 or kamacite and taneite, Fe_3P ± (Fe_3P + Fe_3C) in complex phase relationships. At ~1350 °C, the spherules may have contained a homogeneous Fe–P–S–C melt which separated into two immiscible melts in the 1350–1250 °C interval: a dense Fe–P–C in the core and a less dense Fe–S melts in the rim. The two melts evolved upon further cooling following the paths for the Fe–S and Fe–P–C systems. After the crystallization of pyrrhotitic rim, the Fe–P–C melt parent to the schreibersite zone preserved yet its fluidity; Fe_3P and Fe_3C crystallized between 988 and 952 °C.

The evolution of redox conditions during crystallization of melilite–nepheline paralava melts and their subsequent cooling was reconstructed with reference to the CCO, IW, IM, and MW buffer equilibria from the inferred crystallization temperatures of the reduced mineral assemblages.

The formation of high-temperature reducing mineral assemblages during multi-stage underground coal fires may have been as follows. Thermal alteration of some low-permeable overburden domains above the fire foci was possible with very little to zero air oxygen access, by conductive heat transfer from adjacent burning parts of the coal seams. The gas flow in those zones, with the lack of atmospheric oxygen and water but excess of atomic carbon, was apparently controlled by the CCO buffer. The mineral assemblages with troilite, metallic iron, iron phosphides, and cohenite crystallized from droplets of immiscible Fe–S, Fe–P, and Fe–P–S–C liquids in high-temperature and extremely reducing conditions.

Author Contributions: Conceptualization and investigation, I.S.P.; field sampling, writing, review, and editing, all authors; visualization, E.A.S. All authors have read and agreed to the published version of the manuscript.

Funding: The study was funded by grant 23–27–00031 from the Russian Science Foundation (RSF).

Acknowledgments: We appreciate the collaboration of our colleagues in analytical work: Yu.D. Shcherbakov (IGC, Irkutsk), A.G. Chueshova (IGC, Irkutsk), and O.Yu. Belozerova (IGC, Irkutsk) for SEM-EDS measurements.

Conflicts of Interest: The authors declare no conflict of interest.

References

1. Peretyazhko, I.S.; Savina, E.A.; Khromova, E.A. Minerals of the rhönite-kuratite series in paralavas from a new combustion metamorphic complex of Choir–Nyalga Basin (Central Mongolia): Chemistry, mineral assemblages, and formation conditions. *Min. Mag.* **2017**, 81(4), 949–974. https://doi.org/10.1180/minmag.2016.080.143
2. Peretyazhko, I.S.; Savina, E.A.; Khromova, E.A.; Karmanov, N.S.; Ivanov, A.V. Unique clinkers and paralavas from a new Nyalga combustion metamorphic complex in central Mongolia: Mineralogy, geochemistry, and genesis. *Petrology* **2018**, 26, 181–211. https://doi.org/10.1134/S0869591118020054
3. Savina, E.A.; Peretyazhko, I.S.; Khromova, E.A.; Glushkova, V.E. Melted rocks (clinkers and paralavas) of Khamaryn-Khural-Khiid combustion metamorphic complex in Eastern Mongolia: Mineralogy, geochemistry and genesis. *Petrology* **2020**, 28, 431–457. https://doi.org/10.1134/S0869591120050057
4. Savina, E.A.; Peretyazhko, I.S. Cristobalite Clinker and Paralavas of Ferroan and Melilite–Nepheline Types in the Khamaryn-Khural–Khiid Combustion Methamorphic Complex, East Mongolia: Formation

Conditions and Processes. *Russ. Geol. Geophys.* **2023**, 64(12), 1408–1429. https://doi.org/10.2113/RGG20234603

5. Peretyazhko I.S., Savina E.A. Melting processes of pelitic rocks in combustion metamorphic complexes of Mongolia: mineral chemistry, Raman spectroscopy, formation conditions of mullite, silicate spinel, silica polymorphs, and cordierite-group minerals. *Geoscience* **2023**, 13:377. https://doi.org/10.3390/geosciences13120377
6. Peretyazhko I.S., Savina E.A., Khromova E.A. Low–pressure (> 4 MPa) and high–temperature (> 1250°C) incongruent melting of marly limestone: formation of carbonate melt and melilite–nepheline paralava in the Khamaryn–Khural–Khiid combustion metamorphic complex, East Mongolia. *Contrib. Miner. Petrol.* **2021**, 176:38. https://doi.org/10.1007/s00410-021-01794-5
7. Glushkova, V.E.; Peretyazhko, I.S.; Savina, E.A.; Khromova, E.A. Olivine-group minerals in melilite-nepheline paralava of combustion metamorphic complexes in Mongolia. *Zap. Ross. Mineral. Obs.* **2023**, 1, 61–77. (in Russian) https://doi.org/10.31857/S0869605523010045
8. Glushkova, V.E.; Peretyazhko, I.S.; Savina, E.A.; Khromova, E.A. Rock-forming minerals in paralava of combustion metamorphic complexes in Mongolia. *Zap. Ross. Mineral. Obs.* **2023**, 4, 65–83. (in Russian) https://doi.org/10.31857/S0869605523040056
9. Lavrent'ev, Yu.G., Karmanov, N.S., Usova, L.V. Electron probe microanalysis of minerals: Microanalyzer or scanning electron microscope ? *Russ. Geol. Geophys.* **2015**, 56 (8), 1154–1161 (in Russian). https://doi.org/10.1016/j.rgg.2015.07.006
10. Peretyazhko, I.S. CRYSTAL – applied software for mineralogist, petrologist, and geochemists [in Russian]. *Zap. Ross. Mineral. Obs.* 1996, 3, 141–148. (in Russian)
11. Shendrik, R.Y.; Plechov, P.Y.; Smirnov, S.Z. ArDI – the system of mineral vibrational spectroscopy data processing and analysis. *New Data on Minerals* **2024**, 58, 2–35. https://doi.org/10.25993/FM.2024.58.2024.008
12. Lafuente, B.; Downs, R.T.; Yang, H.; Stone, N. The power of databases: The RRUFF project. In Highlights in Mineralogical Crystallography. Walter de Gruyter GmbH, 2016; pp. 1-29. https://doi.org/10.1515/9783110417104-003
13. Li, X.; Chen, Yi.; Xu Tang, Xu.; Lixin Gu, L.; Yuan, J.; Su, W.; Tian, H.; Luo, H.; Cai, S.; Sridhar Komarneni, S. Thermally induced phase transition of troilite during micro-raman spectroscopy analysis. *Iracus* **2023**, 390:115299. https://doi.org/10.1016/j.icarus.2022.115299
14. Walder, P.; Pelton, A.D. Thermodynamic Modeling of the Fe-S System. *J. Phase Equilib. Diffus.* **2005**, 26(1), 23–38, http://dx.doi.org/10.1361/15477030522455
15. Sheshin, D.; Decretov, S.A. Critical Assessment and Thermodynamic Modeling of the Fe-O-S System. *J. Phase Equilib. Diffus.* **2015**, 36(3), 224–240, http://dx.doi.org/10.1007/s11669-015-0376-4
16. Pirim, C.; Pasek, M.A.; Sokolov, D.A.; Sidorov, A.N.; Gann, R.D.; Orlando, T.M. Investigation of schreibersite and intrinsic oxidation products from Sikhote-Alin, Seymchan, and Odessa meteorites and Fe_3P and Fe_2NiP synthetic. *Geoch. Cosmochim. Acta* **2014**, 140, 2599–274. http://dx.doi.org/10.1016/j.gca.2014.05.027
17. Wang, X.; Zhang, S.; Li, J.; Xu, J., Wang, X., 2014. Fabrication of Fe/Fe_3C@porous carbon sheets from biomass and their application for simultaneous reduction and adsorption of uranium(VI) from solution. *Inorg. Chem. Front.* **2014**, 1, 641–648, http://dx.doi.org/10.1039/c4qi00071d
18. Bina, C.R. Lower mantle mineralogy and the geophysical perspective. In Ultrahigh Pressure Mineralogy: Physics and Chemistry of the Earth's Deep Interior. Walter de Gruyter GmbH, **2019** 205–240.
19. Kiseeva, E.S.; Korolev, N.; Koemets, I.; Zedgenizov, D.A.; Unitt, R.; McCammon, C.; Aslandukova, A.; Khandarkhaeva, S., Fedotenko, T.; Glazyrin, K.; Bessas, D.; Aprilis, G.; Chumakov, A.I.; Kagi, H.; Dubrovinsky, L. Subduction-related oxidation of the sublithospheric mantle evidenced by ferropericlase and magnesiowüstite diamond inclusions. *Nature Comm.* **2021**, 13:7517, 1–8. https://doi.org/10.1038/s41467-022-35110-x
20. Boiocchi, M.; Caucia, F., Merli, M.; Prella, D.; Ungaretti, L. Crystal-chemical reasons for the immiscibility of periclase and wüstite under lithospheric P, T conditions. *Eur. J. Mineral.* **2001**, 13, 871–881. https://doi.org/10.1127/0935-1221/2001/0013/0871
21. Tupitsin, A.A.; Yas'ko, S.V.; Bychinsky, V.A.; Peretyazhko, I.S.; Glushkova, V.E. Thermodynamic assessment of the phase diagrams of calcite and CaO–$CaCO_3$ system. *Materialia* **2024**, 34:102106. https://doi.org/10.1016/j.mtla.2024.102106
22. Samoilova, O.; Markovets, L. Thermodynamic Modeling of Phase Equilibria in the FeO-MgO-Al_2O_3 System. *Materials Science Forum* **2020**, 989:3–9. https://doi.org/10.4028/www.scientific.net/MSF.989.3
23. Schenck, H.; Pfaff, W. Das system eisen(II)–oxyd–magnesiumoxyd und seine verteilungsgleichgewichte mit flüssigem eisen bei 1520 bis 1750 °C. *Arch. Eisenhüttenwes* **1961**, 32, 741–751. (in German)
24. Scheel, R. Gleichgewichte im system CaO–MgO–FeOn bei gegenwart von metallischem eisen, Sprechsaal für Keramik, Glas. *Baustoffe* **1975**, 108, 685–686. (in German)

25. Vereshchagin, O.S.; Khmelnitskaya, M.O.; Murashko, M.N.; Vapnik, Y.; Zaitsev, A.N.; Vlasenko, N.S.; Shilovskikh, V.V.; Britvin, S.N. Reduced mineral assemblages of superficial origin in west-central Jordan. *Mineral. Petrol.* **2024**, 118, 305–319. https://doi.org/10.1007/s00710-024-00851-8
26. Vereshchagin, O.S.; Khmelnitskaya, M.O.; Kamaeva, L.V.; Vlasenko, N.S.; Pankin, D.V.; Bocharov, V.N., Britvin, S.N. Telluric iron assemblages as a source of prebiotic phosphorus on the early Earth: Insights from Disko Island, Greenland. *Geosci. Front.* **2024**, 15:101870. https://doi.org/10.1016/j.gsf.2024.101870
27. Britvin, S.N.; Murashko, M.N.; Vapnik, Y.; Polekhovsky, Y. S.; Krivovichev, S.V.; Vereshchagin, O.S.; Shilovskikh, V.V.; Krzhizhanovskaya, M.G. Negevite, the pyrite-type NiP_2, a new terrestrial phosphide. *Am. Mineral.* **2020**, 105, 422–427. https://doi.org/ 10.2138/am-2020-7192
28. Britvin, S.N.; Rudashevsky, N.S.; Krivovichev, S.V.; Burns, P.; Polekhovsky, Y.S. Allabogdanite, $(Fe,Ni)_2P$, a new mineral from the Onello meteorite: the occurrence and crystal structure. *Am. Mineral.* **2002**, 87, 1245–1249. https://doi.org/10.2138/am-2002-8-924
29. Britvin, S.N.; Shilovskikh, V.V.; Pagano, R., Vlasenko, N.S.; Zaitsev, A.N.; Krzhizhanovskaya, M.G.; Lozhkin M.S.; Andrey A. Zolotarev A.A.; Gurzhiy V.V. 2019. Allabogdanite, the high-pressure polymorph of $(Fe,Ni)_2P$, a stishovite-grade indicator of impact processes in the Fe–Ni–P system. *Sci Rep.* **2019**, 9, 1–8. https://doi.org/10.1038/s41598-018-37795-x
30. Britvin, S.N., Vapnik, Y.; Polekhovsky, Y.S.; Krivovichev, S.V.; Krzhizhanovkaya, M.G.; Gorelova, L.A.; Vereshchagin, O.S.; Shilovskikh, V.V.; and Zaitsev, A.N. Murashkoite, FeP, a new terrestrial phosphide from pyrometamorphic rocks of the Hatrurim Formation, South Levant. *Mineral. Petrol.* **2019**, 113, 237–248. https://doi.org/10.1007/s00710-018-0647-y
31. Britvin, S.N.; Murashko, M.N.; Vapnik, Ye.; Polekhovsky, Yu.S.; Krivovichev, S.V.; Vereshchagin, O.S.; Vlasenko, N.S.; Shilovskikh, V.V.; Zaitsev, A.N., 2019. Zuktamrurite, FeP_2, a new mineral, the phosphide analogue of löllingite, $FeAs_2$. *Physics and Chemistry of Minerals* **2019**, 46, 361–369. https://doi.org/10.1007/s00269-018-1008-4
32. Britvin, S.N.; Vereshchagin, O.S.; Shilovskikh, V.V.; Krzhizhanovskaya, M.G.; Gorelova, L.A.; Vlasenko, N. S.; Pakhomova, A.S.; Zaitsev, A.N.; Zolotarev, A.A.; Bykov, M.; Lozhkin, M.S.; Nestola, Fabrizio. Discovery of terrestrial allabogdanite $(Fe,Ni)_2P$, and the effect of Ni and Mo substitution on the barringerite allabogdanite high-pressure transition. *Am. Mineral.* **2021**, 106, 944–952. https://doi.org/10.2138/am-2021-7621
33. Britvin, S.N.; Murashko, M.N.; Vapnik, Ye.; Polekhovsky, Yu.S.; Krivovichev, S.V.; Krzhizhanovskaya, M.G.; Vereshchagin, O.S.; Shilovskikh, V.V.; Vlasenko N.S. Transjordanite, Ni_2P, a new terrestrial and meteoritic phosphide, and natural solid solutions barringerite–transjordanite (hexagonal Fe_2P–Ni_2P). *Am. Mineral.* **2020**, 105, 428–436. DOI:10.2138/am-2020-7275
34. Britvin, S.N.; Murashko, M.N.; Vapnik Ye.; Polekhovsky Yu.S.; Krivovichev S.V.; Vereshchagin O.S.; Shilovskikh; V.V.; Vlasenko, N.S.; Krzhizhanovskaya, M.G. Halamishite, Ni_5P_4, a new terrestrial phosphide in the Ni–P system. *Physics and Chemistry of Minerals* **2020**, 3. https://doi.org/10.1007/s00269-019-01073-7
35. Britvin, S.N.; Murashko, M.N.; Krzhizhanovskaya, M.G.; Vereshchagin, O.S.; Vapnik Ye.; Shilovskikh, V.V.; Lozhkin, M.S.; Obolonskaya, E.V. Nazarovite, $Ni_{12}P_5$, a new terrestrial and meteoritic mineral structurally related to nickelphosphide, Ni_3P. *Am. Mineral.* **2022**. https://doi.org/10.2138/am-2022-8219
36. Britvin, S.N.; Murashko, M.N.; Vereshchagin, O.S.; Vapnik, Ye.; Shilovskikh, V.V.; Vlasenko, N.S.; Permyakov, V.V. Expanding the speciation of terrestrial molybdenum: discovery of polekhovskyite, $MoNiP_2$, and insights into the sources of Mo-phosphides in the Dead Sea Transform area. *Am. Mineral.* **2022**. https://doi.org/10.2138/am-2022-8261.
37. Galuskin E.V.; Kusz, J.; Galuskina, I.O.; Książek, M.; Vapnik, Y.; Zieliński, G., 2023. Discovery of terrestrial andreyivanovite, FeCrP, and the effect of Cr and V substitution on the low-pressure barringerite-allabogdanite transition. *Am. Mineral.* **2023**, 108 (8). 1506–1515. https://doi.org/10.2138/am-2022-8647
38. Dera, P. ; Lavina, B.; Borkowski, L.A.; Prakapenka, V.B.; Sutton, S.R. ; Rivers, M.L.; Downs, R.T.; Boctor, N.Z.; Prewitt, C.T. Structure and behavior of the barringerite Ni end-member, Ni_2P, at deep Earth conditions and implications for natural Fe-Ni phosphides in planetary cores. *J. Geophys. Res.* **2009**, 114, B03201. https://doi.org/10.1029/2008JB005944.
39. Litasov, K.D.; Bekker, T.B.; Sagatov, N.E.; Gavryushkin, P.N.; Krinitsyn, P.G.; Kuper, K.E. (Fe,Ni)2P allabogdanite can be an ambient pressure phase in iron meteorites. *Scientific Reports* 2020, 10(1):8956, https://doi.org/10.1038/s41598-020-66039-0
40. Kong, S.; Singh; P.; Sarkar, A.; Viswanathan, G.; Kolen'ko, Yu.V.; Mudryk, Y.; Johnson, D.D,.; Kovnir, K., 2024. Enhancing Properties with Distortion: A Comparative Study of Two Iron Phosphide Fe_2P Polymorphs. *Chem. Mat.* **2024**, 36(3), 1665–1677. https://doi.org/10.1021/acs.chemmater.3c03003
41. Miettinen, J.; Vassilev, G., 2014. Thermodynamic Description of Ternary Fe-X-P Systems. Part 1: Fe-Cr-P. *J. Phase Equilib. Diffus.* **2014**, 35, 458–468. https://doi.org/10.1007/s11669-014-0314-x
42. Jones, H.; Drake, M.J. Experimental investigations of trace element fractionation in iron meteorites, II: The influence of sulfur. *Geoch. Cosmochim. Acta* **1983**, 47, 1199–1209.

43. Raghavan, V. The Fe-P-S System. *In Phase Diagrams of Ternary Iron Alloys* **1988**, 2, 209–217. Indian National Scientific Documentation Centre, New Delhi, India.
44. Chabot, N.L.; Drake, M.J. Crystallization of magmatic iron meteorites: The effects of phosphorus and liquid immiscibility. *Meteorit. Planet. Sci.* **2000**, 35(4), 807–816. https://doi.org/10.1111/j.1945-5100.2000.tb01464.x
45. Shim, J.H.; Oh, C.S.; Lee, D.N., 2000. Thermodynamic Assessment of the Fe-C-P System. *Zeitschrift für Metallkunde* 2000, 91(2), 114–120. https://doi.org/10.1515/ijmr-2000-910203
46. Schurmann, E.; Hensgen, U.; Schweinichen, J. Melt Equilibrium of the Ternary Systems Fe-C-Si and Fe-C-P. *Geissereiforsch.* 1984, 36(4), 121–129. (in German)
47. Sokol, E.V., Maksimova, N.V., Nigmatulina, E.N., Sharygin, V.V., Kalugin V.M. (Eds.). Combustion Metamorphism **2005**, Izd. SO RAN, Novosibirsk. (in Russian)